Available online at www.sciencedirect.com
ScienceDirect
Journal of Computational Physics 227 (2008) 4543–4562
JOURNAL OF COMPUTATIONAL PHYSICS
www.elsevier.com/locate/jcp

A high-order tangential basis algorithm for electromagnetic scattering by curved surfaces

M. Ganesh [a,*], S.C. Hawkins [b]

[a] Department of Mathematical and Computer Sciences, Colorado School of Mines, Golden, CO 80401, United States
[b] School of Mathematics and Statistics, University of New South Wales, Sydney, NSW 2052, Australia

Received 24 June 2007; received in revised form 8 January 2008; accepted 10 January 2008
Available online 26 January 2008

Abstract

We describe, analyze, and demonstrate a high-order spectrally accurate surface integral algorithm for simulating time-harmonic electromagnetic waves scattered by a class of deterministic and stochastic perfectly conducting three-dimensional obstacles. A key feature of our method is spectrally accurate approximation of the tangential surface current using a new set of tangential basis functions. The construction of spectrally accurate tangential basis functions allows a one-third reduction in the number of unknowns required compared with algorithms using non-tangential basis functions. The spectral accuracy of the algorithm leads to discretized systems with substantially fewer unknowns than required by many industrial standard algorithms, which use, for example, the method of moments combined with fast solvers based on the fast multipole method. We demonstrate our algorithm by simulating electromagnetic waves scattered by medium-sized obstacles (diameter up to 50 times the incident wavelength) using a direct solver (in a small parallel cluster computing environment). The ability to use a direct solver is a tremendous advantage for monostatic radar cross section computations, where thousands of linear systems, with one electromagnetic scattering matrix but many right hand sides (induced by many transmitters) must be solved.
Published by Elsevier Inc.

MSC: 65R20; 65N35

Keywords: Tangential vector basis; Electromagnetic scattering; Maxwell's equations; Radar cross section; Monostatic; Bistatic; Boundary integral; Spectral; Galerkin; Quadrature

1. Introduction

Understanding of many physical phenomena and processes in atmospheric science, climatology, and astronomy can be enhanced through simulation of electromagnetic waves scattered by non-convex particles such as atmospheric aerosols, dust in planetary rings, ice crystals, or interstellar dust [15,30,37]. Scattering simulations also play an important role in medical sciences because scattering is an important tool, for exam-

* Corresponding author. Tel.: +1 303 273 3927; fax: +1 303 273 3975.
E-mail addresses: mganesh@mines.edu (M. Ganesh), stuart@maths.unsw.edu.au (S.C. Hawkins).

0021-9991/$ - see front matter Published by Elsevier Inc.
doi:10.1016/j.jcp.2008.01.016

ple, in classifying bi-concave blood cells [22,40] and in image-guided neurosurgery using medical imaging, for example, of tumor models [12,21,41,42]. These obstacles are in general dielectric. However, developing algorithms to simulate scattering by such perfectly conducting bodies is a crucial first step towards development of spectrally accurate algorithms for electromagnetic scattering by three-dimensional dielectric bodies.

In this work we construct tangential vector basis functions on the surfaces of these particles, and present a spectrally accurate high-order algorithm to simulate the interaction of electromagnetic waves with a perfectly conducting three-dimensional obstacle D situated in a homogeneous medium with vanishing conductivity, the free space permittivity $\epsilon_0 = 10^7/(4\pi c^2)$ F/m and permeability $\mu_0 = 4\pi \times 10^{-7}$ H/m, where $c = 299,792,458$ m/s is the speed of light. We develop the algorithm using a class of surface parametrization (described in Section 2.2) that includes a major class of model deterministic and stochastic surfaces used in the literature.

The electromagnetic waves, with angular frequency ω (rad/s) and wavelength $\lambda = 2\pi c/\omega$ (m), scattered by D are described by the electric field intensity $\boldsymbol{\mathcal{E}}$ with units V/m and the magnetic field intensity $\boldsymbol{\mathcal{H}}$ with units A/m [34, Section 1.8]. In this work we consider time harmonic electromagnetic waves, which can be represented as

$$\boldsymbol{\mathcal{E}}(\boldsymbol{x},t) = \frac{1}{\sqrt{\epsilon_0}}\mathrm{Re}\{\boldsymbol{E}(\boldsymbol{x})\mathrm{e}^{-\mathrm{i}\omega t}\}, \quad \boldsymbol{\mathcal{H}}(\boldsymbol{x},t) = \frac{1}{\sqrt{\mu_0}}\mathrm{Re}\{\boldsymbol{H}(\boldsymbol{x})\mathrm{e}^{-\mathrm{i}\omega t}\}, \quad \boldsymbol{x} \in \mathbb{R}^3 \setminus \overline{D}. \tag{1.1}$$

The complex vector fields $\boldsymbol{E}$, $\boldsymbol{H}$, which describe the magnitude, direction and phase of the electric and magnetic field intensities, satisfy the time harmonic Maxwell equations [9, p. 154]

$$\mathbf{curl}\,\boldsymbol{E}(\boldsymbol{x}) - \mathrm{i}k\boldsymbol{H}(\boldsymbol{x}) = \boldsymbol{0}, \quad \mathbf{curl}\,\boldsymbol{H}(\boldsymbol{x}) + \mathrm{i}k\boldsymbol{E}(\boldsymbol{x}) = \boldsymbol{0}, \qquad \boldsymbol{x} \in \mathbb{R}^3 \setminus \overline{D}, \tag{1.2}$$

with wave number $k = 2\pi/\lambda$ rad/m, the Silver–Müller radiation condition

$$\lim_{|\boldsymbol{x}|\to\infty} [\boldsymbol{H}(\boldsymbol{x}) \times \boldsymbol{x} - |\,\boldsymbol{x}\,|\,\boldsymbol{E}(\boldsymbol{x})] = \boldsymbol{0}, \tag{1.3}$$

and the perfect conductor boundary condition

$$\boldsymbol{n}(\boldsymbol{x}) \times \boldsymbol{E}(\boldsymbol{x}) = -\boldsymbol{n}(\boldsymbol{x}) \times \boldsymbol{E}^{\mathrm{inc}}(\boldsymbol{x}) =: \boldsymbol{f}(\boldsymbol{x}), \quad \boldsymbol{x} \in \partial D, \tag{1.4}$$

where $\boldsymbol{n}(\boldsymbol{x})$ denotes the unit outward normal at $\boldsymbol{x}$ on the surface ∂D of D and $\boldsymbol{E}^{\mathrm{inc}}$ is the incident electric field. In our experiments the incident field $\boldsymbol{E}^{\mathrm{inc}}$, $\boldsymbol{H}^{\mathrm{inc}}$ is the plane wave

$$\boldsymbol{E}^{\mathrm{inc}}(\boldsymbol{x}) = \mathrm{i}k\hat{\boldsymbol{p}}_0\mathrm{e}^{\mathrm{i}k\boldsymbol{x}\cdot\hat{\boldsymbol{d}}_0}, \quad \boldsymbol{H}^{\mathrm{inc}}(\boldsymbol{x}) = \mathrm{i}k[\hat{\boldsymbol{d}}_0 \times \hat{\boldsymbol{p}}_0]\mathrm{e}^{\mathrm{i}k\boldsymbol{x}\cdot\hat{\boldsymbol{d}}_0}, \qquad \hat{\boldsymbol{d}}_0 \perp \hat{\boldsymbol{p}}_0, \tag{1.5}$$

where $\hat{\boldsymbol{d}}_0$ is the direction of the plane wave and $\hat{\boldsymbol{p}}_0$ its polarization.

Of particular interest is the radar cross section (RCS) [24] of the obstacle D, measured by a receiver with polarization $\hat{\boldsymbol{p}}_1$ situated in the direction

$$\hat{\boldsymbol{x}} = \boldsymbol{p}(\theta,\phi) = (\sin\theta\cos\phi, \sin\theta\sin\phi, \cos\theta)^{\mathrm{T}}, \qquad \hat{\boldsymbol{x}} \in \partial B, \tag{1.6}$$

where ∂B denotes the unit sphere, which is defined as

$$\sigma(\hat{\boldsymbol{x}}) = 4\pi\,|\,\boldsymbol{E}_\infty(\hat{\boldsymbol{x}}) \cdot \hat{\boldsymbol{p}}_1|^2/k^2, \qquad \boldsymbol{E}_\infty(\hat{\boldsymbol{x}}) = \lim_{r\to\infty} \boldsymbol{E}(r\hat{\boldsymbol{x}})\mathrm{e}^{-\mathrm{i}kr}r. \tag{1.7}$$

$\boldsymbol{E}_\infty$ is the electric far field. Two types of RCS are of particular interest: (i) The RCS for all directions $\hat{\boldsymbol{x}}$, with a fixed incident direction $\hat{\boldsymbol{d}}_0$; (ii) The RCS for all directions $\hat{\boldsymbol{x}}$, with varying incident directions $\hat{\boldsymbol{d}}_0 = -\hat{\boldsymbol{x}}$. These are the bistatic and monostatic RCS respectively [24]. Co-location of the transmitter and receiver in the monostatic RCS requires, unlike in the bistatic case, solution of the Maxwell equations with thousands of distinct boundary conditions of the form (1.4).

The Mie-series solution is useful for checking the accuracy of our algorithm on spherical scatterers. For checking the accuracy of our algorithm on non-spherical scatterers, we also consider the boundary conditions

$$\boldsymbol{f}(\boldsymbol{x}) := \boldsymbol{n}(\boldsymbol{x}) \times \boldsymbol{E}^{\mathrm{ED}}(\boldsymbol{x}), \qquad \boldsymbol{f}(\boldsymbol{x}) := \boldsymbol{n}(\boldsymbol{x}) \times \boldsymbol{E}^{\mathrm{MD}}(\boldsymbol{x}), \quad \boldsymbol{x} \in \partial D, \tag{1.8}$$

where the boundary data $\boldsymbol{f}$ is induced by the electric and magnetic dipole solutions $\boldsymbol{E}^{\mathrm{ED}}, \boldsymbol{H}^{\mathrm{ED}}$ and $\boldsymbol{E}^{\mathrm{MD}}, \boldsymbol{H}^{\mathrm{MD}}$ of the Maxwell equations, which describe radiation from a point source with polarization $\hat{\boldsymbol{p}}_{\mathrm{src}}$ located at $\boldsymbol{x}_{\mathrm{src}} \in D$ [9, (6.20), (6.21), p. 163]:

$$\boldsymbol{E}^{\mathrm{ED}}(\boldsymbol{x}) = -\frac{1}{\mathrm{i}k}\,\mathbf{curl}_{\boldsymbol{x}}\mathbf{curl}_{\boldsymbol{x}}\{\hat{\boldsymbol{p}}_{\mathrm{src}}\Phi(\boldsymbol{x},\boldsymbol{x}_{\mathrm{src}})\}, \qquad \boldsymbol{H}^{\mathrm{ED}}(\boldsymbol{x}) = \mathbf{curl}_{\boldsymbol{x}}\{\hat{\boldsymbol{p}}_{\mathrm{src}}\Phi(\boldsymbol{x},\boldsymbol{x}_{\mathrm{src}})\}, \tag{1.9}$$

and

$$\boldsymbol{E}^{\mathrm{MD}}(\boldsymbol{x}) = \mathbf{curl}_{\boldsymbol{x}}\{\hat{\boldsymbol{p}}_{\mathrm{src}}\Phi(\boldsymbol{x},\boldsymbol{x}_{\mathrm{src}})\}, \qquad \boldsymbol{H}^{\mathrm{MD}}(\boldsymbol{x}) = \frac{1}{\mathrm{i}k}\mathbf{curl}_{\boldsymbol{x}}\mathbf{curl}_{\boldsymbol{x}}\{\hat{\boldsymbol{p}}_{\mathrm{src}}\Phi(\boldsymbol{x},\boldsymbol{x}_{\mathrm{src}})\}, \tag{1.10}$$

where

$$\Phi(\boldsymbol{x},\boldsymbol{y}) = \frac{1}{4\pi}\,\frac{\mathrm{e}^{\mathrm{i}k|\boldsymbol{x}-\boldsymbol{y}|}}{|\,\boldsymbol{x}-\boldsymbol{y}\,|} \tag{1.11}$$

is the fundamental solution of the Helmholtz equation.

Although scattering problems have a long pedigree, there is substantial interest in establishing reliable, high-order and fast algorithms for their solution. Difficulties arise in this practically important problem due to the shape of curved scattering surfaces and the frequency of the incident wave (or more precisely the electromagnetic size of the scatterers). This is because many established electromagnetic scattering algorithms for small to medium-sized obstacles (say one to one hundred times the incident wavelength) require setting up and solving complex dense linear systems with several thousand to several million unknowns. For example, to compute the bistatic radar cross section of a perfectly conducting sphere of diameter 48 times the incident wavelength at 7.2 GHz, the industrial standard boundary element/method of moments based FISC (Fast Illinois Solver Code) algorithm requires 2,408,448 unknowns to achieve 0.33 dB relative error, measured in a root mean square (RMS) norm [33, p. 29]. Furthermore, as discussed in the preface of [29, p. vi], *the effects of the approximation of smooth boundaries is not well understood for Maxwell's equations*.

For high-frequency problems (with obstacle size tens of thousands of times the incident wavelength) one may use appropriate asymptotics (physical optics or Kirchhoff approximation [27]) for the illuminated region and special approximations for the shadow and transition zones to reduce the number of unknowns and the number of integrals required for the discretization, obtaining accuracy that increases as the wave number k increases (specifically, accuracy $\mathcal{O}(k^{-\alpha})$ for $\alpha > 0$). Such an approach has recently been implemented and analyzed in various ways for high-frequency acoustic scattering (using the Helmholtz equation) by single and multiple two dimensional convex obstacles in [3,5,10,13,20,25] and related references therein. However, for high-frequency acoustic scattering by three-dimensional convex obstacles, one encounters substantial difficulties in using such approximations and computations, for example in finding stationary points of various types, and efficient approximations in shadow and transition regions. For recent but limited progress in this area for acoustic scattering by three-dimensional convex obstacles, we refer to [4,19] and references therein. However, development and realization of a similar asymptotic approach for simulation of scattering by three-dimensional non-convex obstacles is an open problem.

In this work, we use direct (as opposed to asymptotic) methods to develop a spectrally accurate algorithm to simulate the interaction of electromagnetic waves with small to medium electromagnetic-sized deterministic and stochastic obstacles. Spectrally accurate algorithms to approximate the analytic electric and magnetic fields, which are naturally tangential on associated scattering surfaces, have recently been developed in [17,18] and were mathematically proven to yield spectral accuracy. A large set of simulation results in [17,18] demonstrate that the algorithms are more efficient than industrial standard electromagnetic scattering algorithms such as FastScat [7], FISC [33], FE-IE and CARLOS [1], and FERM and CICERO [39], for a class of benchmark obstacles. The methods in [17,18] are based on finite dimensional ansatz spaces that include non-tangential basis functions, leading to the dimension of the ansatz space being *three times* that required for the acoustic counterpart methods in [16] (due to one normal and two tangential components). The algorithms in [17,18] are based on a modification of the standard electric field surface integral reformulation of the Maxwell equations that admits non-tangential approximations to the tangential surface electric field.

The *three times* computational penalty in [17,18] is substantial for medium frequency scattering and for monostatic RCS computations, for which linear systems are to be set up and solved with thousands of different right hand sides, arising due to co-location of the transmitter and receiver. In [18], the penalty is avoided if the scatterer is a sphere, for which spectrally accurate tangential vector basis functions are well known and widely used for the analytic Mie-series solution [9,29]. Algorithms based on ansatz spaces spanned by just

surface tangential vector fields lead to only a *two times* computational penalty compared with their acoustic counterparts [16]. Construction of ansatz spaces spanned by vector basis functions that are tangential on general curved surfaces and development of algorithms utilizing these spaces, in which tangential electric fields can be approximated with spectral accuracy, is a significant challenge.

In this work we describe such ansatz spaces, and subsequently develop a new algorithm that gives high-order spectral accuracy with two-thirds of the unknowns required by the algorithms in [17,18]. We demonstrate this important advancement of the spectrally accurate algorithms in [17,18] with numerical experiments using various deterministic and stochastic surfaces. The reduction in unknowns (and hence reduced memory usage) allows us to simulate electromagnetic waves with the excellent accuracy achieved in [17,18] at frequencies up to one hundred percent higher, using a small cluster computing environment similar to that used in [17,18].

Our ansatz space is based upon tangential vector spherical harmonics that arise via the surface-gradient and surface-curl of spherical harmonics. Such vector spherical harmonics are widely used in Mie series [36, Chapter 9] and T-matrix [28] computations for electromagnetic scattering by spheres and non-spherical particles respectively, where they arise as components of fundamental solutions of the Maxwell equations that are defined throughout the exterior of the scatterer. In our boundary integral equation (BIE) algorithm, transformed vector spherical harmonics (with a tangential-like property on a given non-spherical surface) are used to approximate a vector potential on a spherical reference surface, which yields the exterior field via a surface integral representation. In contrast, in the Mie and T-matrix computations vector spherical harmonics are used to approximate the exterior field throughout the exterior of the scatterer.

The truncated T-matrix is often computed using the null-field method [28]. Null-field method based T-matrix computations are numerically unstable, and round-off errors become significant when the dimension of the truncated T-matrix is large. Consequently, such computations can become divergent for large and/or highly non-spherical particles [28, p. 543]. Such instability problems are avoided by, for example, using slow extended precision arithmetic to minimize the effect of round-off errors [28, p. 544].

It is known [26, Section 7.9.4] that numerical instability involved in the null-field method can be avoided by using a BIE to compute the T-matrix. The only disadvantage of using a BIE to compute the T-matrix is that this approach requires solving a large number of (boundary integral) linear systems with a fixed scattering matrix (obtained by discretizing the associated boundary integral operator) but different right hand sides (corresponding to each wave function used in expanding the incident field). Consequently, it is crucial to develop a spectrally accurate scattering algorithm that requires fewer unknowns, allowing utilization of the LU-factorization of the scattering matrix. In this work, we develop such an algorithm, and application of the algorithm to compute the T-matrix in a stable way for various non-spherical obstacles will be considered in a future work.

2. Surface integral equation reformulations

In this section, we describe analytical reformulations of the electromagnetic scattering problem involving surface integral operators, and a class of parametrization of the scatterer's surface. Let $\underline{T}(\partial D)$ and $\underline{T}^{0,\alpha}(\partial D)$ denote the space of all continuous and uniformly Hölder continuous tangential vector fields on ∂D with the supremum and Hölder norm respectively. Let $\underline{T}^r(\partial D)$ denote the subspace of $\underline{T}(\partial D)$ consisting of all r-times continuously differentiable functions on ∂D with norm $\|\cdot\|_{r,\infty,\partial D}$. (If $r = 0$, we drop the notation r in spaces and norms.) The spaces $\underline{T}(\partial B)$ and $\underline{T}^r(\partial B)$ are defined similarly with ∂D replaced by ∂B.

2.1. Surface integral operators and equations

The unique radiating exterior solution $\boldsymbol{E}, \boldsymbol{H}$ of (1.2) satisfying the boundary condition (1.4), (1.5) or (1.8)–(1.10) can be represented as [8, Theorem 4.19, p. 126]

$$\boldsymbol{E}(\boldsymbol{x}) = \mathbf{curl} \int_{\partial D} \Phi(\boldsymbol{x}, \boldsymbol{y}) \boldsymbol{w}(\boldsymbol{y}) \, \mathrm{d}s(\boldsymbol{y}), \tag{2.1}$$

$$\boldsymbol{H}(\boldsymbol{x}) = \frac{1}{\mathrm{i}k} \mathbf{curl}\, \boldsymbol{E}(\boldsymbol{x}) \tag{2.2}$$

for $\boldsymbol{x} \in \mathbb{R}^3 \setminus \overline{D}$, provided $\boldsymbol{w} \in \underline{T}^{0,\alpha}(\partial D)$ for $0 < \alpha < 1$ solves the surface integral equation

$$\boldsymbol{w}(\boldsymbol{x}) + (\mathscr{M}\boldsymbol{w})(\boldsymbol{x}) = 2\boldsymbol{f}(\boldsymbol{x}), \tag{2.3}$$

where $\mathscr{M} : \underline{T}(\partial D) \to \underline{T}^{0,\alpha}(\partial D)$ is the bounded magnetic dipole operator [8, p. 167], given by

$$(\mathscr{M}\boldsymbol{a})(\boldsymbol{x}) = 2\int_{\partial D} \boldsymbol{n}(\boldsymbol{x}) \times \mathbf{curl}_{\boldsymbol{x}}\{\Phi(\boldsymbol{x},\boldsymbol{y})\boldsymbol{a}(\boldsymbol{y})\}\,\mathrm{d}s(\boldsymbol{y}), \quad \boldsymbol{x} \in \partial D. \tag{2.4}$$

Restriction of the density $\boldsymbol{a}$ in (2.4) to tangential fields on ∂D reduces the order of singularity of the operator. The solution $\boldsymbol{w}$ of (2.3) is tangential, because the boundary data (1.4), (1.5) and (1.8)–(1.10) are tangential on ∂D. Eq. (2.3) has a unique solution provided the wave number k is not an interior Maxwell eigenvalue [8, Theorem 4.23]. We assume throughout this paper that k is not an interior Maxwell eigenvalue. For $\boldsymbol{a} \in \underline{T}(\partial D)$, we have the following asymptotics of the fundamental solution Φ in (1.11) as $|\boldsymbol{x}| \to \infty$ uniformly for all $\boldsymbol{y} \in \partial D$ [9, p. 164]:

$$\mathbf{curl}_{\boldsymbol{x}}\{\boldsymbol{a}(\boldsymbol{y})\Phi(\boldsymbol{x},\boldsymbol{y})\} = \frac{\mathrm{i}k}{4\pi}\frac{\mathrm{e}^{\mathrm{i}k|\boldsymbol{x}|}}{|\boldsymbol{x}|}\left\{\mathrm{e}^{-\mathrm{i}k\hat{\boldsymbol{x}}\cdot\boldsymbol{y}}\hat{\boldsymbol{x}} \times \boldsymbol{a}(\boldsymbol{y}) + \mathrm{O}\left(\frac{|\boldsymbol{a}(\boldsymbol{y})|}{|\boldsymbol{x}|}\right)\right\},$$

where $\hat{\boldsymbol{x}} = \boldsymbol{x}/|\boldsymbol{x}| \in \partial B$. Using the above asymptotics, (1.7), the unique solution $\boldsymbol{w}$ of (2.3), and (2.1), we get a computable representation of the far field pattern $\boldsymbol{E}_\infty$ of $\boldsymbol{E}$,

$$\boldsymbol{E}_\infty(\hat{\boldsymbol{x}}) = \frac{\mathrm{i}k}{4\pi}\int_{\partial D} \mathrm{e}^{-\mathrm{i}k\hat{\boldsymbol{x}}\cdot\boldsymbol{y}}\hat{\boldsymbol{x}} \times \boldsymbol{w}(\boldsymbol{y})\,\mathrm{d}s(\boldsymbol{y}), \quad \hat{\boldsymbol{x}} \in \partial B. \tag{2.5}$$

To describe our spectrally accurate method, it is convenient to separate the kernel of $\mathscr{M}$ in (2.4) into its weakly singular and smooth parts, using the following identity for a tangential function $\boldsymbol{b} \in \underline{T}(\partial D)$ [9, p. 166]:

$$\boldsymbol{n}(\boldsymbol{x}) \times \mathbf{curl}_{\boldsymbol{x}}\{\Phi(\boldsymbol{x},\boldsymbol{y})\boldsymbol{b}(\boldsymbol{y})\} = \mathbf{grad}_{\boldsymbol{x}}\Phi(\boldsymbol{x},\boldsymbol{y})[\boldsymbol{n}(\boldsymbol{x}) - \boldsymbol{n}(\boldsymbol{y})]^{\mathrm{T}}\boldsymbol{b}(\boldsymbol{y}) - \boldsymbol{b}(\boldsymbol{y})\boldsymbol{n}(\boldsymbol{x})^{\mathrm{T}}\mathbf{grad}_{\boldsymbol{x}}\Phi(\boldsymbol{x},\boldsymbol{y}). \tag{2.6}$$

Using (2.4), (2.6) and (1.11), we write

$$\mathscr{M}\boldsymbol{a}(\boldsymbol{x}) = \int_{\partial D}\left[\frac{1}{|\boldsymbol{x}-\boldsymbol{y}|}m_1(\boldsymbol{x},\boldsymbol{y}) + m_2(\boldsymbol{x},\boldsymbol{y})\right]\boldsymbol{a}(\boldsymbol{y})\,\mathrm{d}s(\boldsymbol{y}), \quad \boldsymbol{x} \in \partial D, \tag{2.7}$$

where for $i = 1, 2$,

$$m_i(\boldsymbol{x},\boldsymbol{y}) = m_{i,1}(\boldsymbol{x},\boldsymbol{y})\frac{1}{|\boldsymbol{x}-\boldsymbol{y}|^2}(\boldsymbol{x}-\boldsymbol{y})[\boldsymbol{n}(\boldsymbol{x}) - \boldsymbol{n}(\boldsymbol{y})]^{\mathrm{T}} + m_{i,2}(\boldsymbol{x},\boldsymbol{y})\frac{1}{|\boldsymbol{x}-\boldsymbol{y}|^2}\boldsymbol{n}(\boldsymbol{x})^{\mathrm{T}}(\boldsymbol{x}-\boldsymbol{y})I + m_{i,3}(\boldsymbol{x},\boldsymbol{y}), \tag{2.8}$$

with I being the 3×3 identity matrix, $m_{2,3} = 0$, the 3×3 zero matrix, and

$$\begin{aligned}
&m_{1,1}(\boldsymbol{x},\boldsymbol{y}) = -\frac{1}{2\pi}t(\boldsymbol{x},\boldsymbol{y}), \qquad m_{1,2}(\boldsymbol{x},\boldsymbol{y}) = \frac{1}{2\pi}t(\boldsymbol{x},\boldsymbol{y}),\\
&m_{1,3}(\boldsymbol{x},\boldsymbol{y}) = \frac{1}{2\pi}ks(\boldsymbol{x},\boldsymbol{y})[\boldsymbol{n}(\boldsymbol{x})^{\mathrm{T}}(\boldsymbol{x}-\boldsymbol{y})I - (\boldsymbol{x}-\boldsymbol{y})(\boldsymbol{n}(\boldsymbol{x}) - \boldsymbol{n}(\boldsymbol{y}))^{\mathrm{T}}],\\
&m_{2,1}(\boldsymbol{x},\boldsymbol{y}) = \frac{1}{2\pi}[\mathrm{i}kt(\boldsymbol{x},\boldsymbol{y}) - \mathrm{i}s(\boldsymbol{x},\boldsymbol{y})], \qquad m_{2,2}(\boldsymbol{x},\boldsymbol{y}) = \frac{1}{2\pi}[\mathrm{i}s(\boldsymbol{x},\boldsymbol{y}) - \mathrm{i}kt(\boldsymbol{x},\boldsymbol{y})],\\
&t(\boldsymbol{x},\boldsymbol{y}) = \cos(k|\boldsymbol{x}-\boldsymbol{y}|), \qquad s(\boldsymbol{x},\boldsymbol{y}) = \begin{cases}\sin(k|\boldsymbol{x}-\boldsymbol{y}|)/|\boldsymbol{x}-\boldsymbol{y}|, & \text{if } \boldsymbol{x} \neq \boldsymbol{y},\\ k, & \text{if } \boldsymbol{x} = \boldsymbol{y}.\end{cases}
\end{aligned} \tag{2.9}$$

Each $m_{i,j}$ $(i = 1, 2,\ j = 1, 2, 3)$ is infinitely differentiable on $\mathbb{R}^3 \times \mathbb{R}^3$.

2.2. Parametrization of the scattering surface

A clearly described parametrization of the obstacle (based on a reference domain or surface) is essential for computer implementation of any algorithm based on a surface integral equation such as (2.3), (2.4). In particular, our main interest is to develop spectrally accurate algorithms for a well defined class of parametrizations that include standard evolving surface representations for reconstruction techniques in inverse scattering (for example, see [9, p. 115; 11, p. R111; 42, p. 1513] and related references therein), and all of the interesting

deterministic and stochastic obstacles mentioned in Section 1, which arise in various applications. We start describing the surface of the obstacle D by recalling a quote from [11, p. R111]: *A popular way of parameterizing surfaces is to use a set of suitable basis functions such as the spherical harmonics*. The spherical harmonics are defined for $\hat{\boldsymbol{x}} \in \partial B$, using (1.6), as

$$Y_{l,j}(\hat{\boldsymbol{x}}) = Y_{l,j}(\theta,\phi) = (-1)^{(j+|j|)/2}\sqrt{\frac{2l+1}{4\pi}\frac{(l-|\,j\,|)!}{(l+|\,j\,|)!}}P_l^{|j|}(\cos\theta)\mathrm{e}^{\mathrm{i}j\phi}, \quad l = 0,1,2,\ldots,|\,j\,| \leqslant l, \tag{2.10}$$

where the $P_l^{|j|}$ are the associated Legendre functions. The spherical coordinate system used in (2.10) with polar angle θ and azimuthal angle ϕ can be used to parametrize ∂D, for example, by choosing a suitable point inside D as origin.

Using the polar and azimuthal angles, we assume that each point $\hat{\boldsymbol{x}}$ on ∂D can be represented as

$$\hat{\boldsymbol{x}} = (x,y,z)^{\mathrm{T}} = (q_1(\theta,\phi), q_2(\theta,\phi), q_3(\theta,\phi))^{\mathrm{T}}, \qquad (x,y,z)^{\mathrm{T}} \in \partial D, \quad \theta,\phi \in \mathbb{R} \tag{2.11}$$

for some nonlinear functionals $q_j : \mathbb{R}^2 \to \mathbb{R}$, for $j = 1,2,3$ that yield, via $\boldsymbol{p}$ in (1.6), a bijective parametrization map $\boldsymbol{q} : \partial B \to \partial D$. In fact, it is sufficient to know a suitable approximation to the parametrization map $\boldsymbol{q}$, for example, based on the Fourier (Laplace) coefficients of q_j for $j = 1,2,3$ with respect to the spherical harmonics expansion.

Many interesting and practically important scatterers can be described in this way, including Gaussian random particles simulating ice crystals (modeled from images obtained by a cloud particle imager) [30], dust particles [37], erythrocytes [22,40], brain tumors [21], all benchmark radar targets in [39], (after converting the material construction coordinates [39] to spherical coordinates [16]), and recently established three-dimensional shape reconstruction surfaces in medical imaging and optical tomography [12,11,41,42].

Restriction to such parametrizations is not a disadvantage in inverse scattering [9] where general qualitative information about scatterers is of greater importance than finer details such as corners and edges. In forward scattering, for simulation of electromagnetic waves exterior to a complex structure, coupling of the finite element and surface integral methods is considered to be the best approach [1,2,23]. Such a coupling is achieved by introducing an artificial interface consisting of a smooth surface that encloses the complex structure, and deriving corresponding Dirichlet-to-Neumann boundary conditions. For efficient computations, the interface should be close to the associated complex structure. For example, such a smooth interface surface can be chosen from those considered in this work. The original problem is then replaced by a problem exterior to the smooth surface coupled with a problem on the remaining bounded domain. The bounded domain problem involving the complex structure can be efficiently solved using various finite element methods [29]. The remaining exterior problem can be solved efficiently using the spectrally accurate algorithm presented in this work.

2.3. Reformulation in spherical coordinates

Using the surface parametrization $\boldsymbol{q}$ we reformulate the surface integral equations (2.3), (2.4) on a spherical reference domain and work in the spherical coordinate system.

We use the bijective parametrization $\boldsymbol{q} : \partial B \to \partial D$ to write (2.3) as

$$\boldsymbol{w}(\boldsymbol{q}(\hat{\boldsymbol{x}})) + (\mathscr{M}\boldsymbol{w})(\boldsymbol{q}(\hat{\boldsymbol{x}})) = 2\boldsymbol{f}(\boldsymbol{q}(\hat{\boldsymbol{x}})), \quad \hat{\boldsymbol{x}} \in \partial B.$$

The surface integral equation (2.3) is then equivalent to

$$\boldsymbol{W}(\hat{\boldsymbol{x}}) + (\mathcal{M}\boldsymbol{W})(\hat{\boldsymbol{x}}) = 2\boldsymbol{F}(\hat{\boldsymbol{x}}), \quad \boldsymbol{W} = \boldsymbol{w}\circ\boldsymbol{q}, \ \boldsymbol{F} = \boldsymbol{f}\circ\boldsymbol{q}, \tag{2.12}$$

where using (2.7), for a given density field $\boldsymbol{A} \in \underline{C}(\partial B)$,

$$\mathcal{M}\boldsymbol{A}(\hat{\boldsymbol{x}}) = \mathcal{M}_1\boldsymbol{A}(\hat{\boldsymbol{x}}) + \mathcal{M}_2\boldsymbol{A}(\hat{\boldsymbol{x}}), \quad \hat{\boldsymbol{x}} \in \partial B, \tag{2.13}$$

with

$$\mathcal{M}_1\boldsymbol{A}(\hat{\boldsymbol{x}}) = \int_{\partial B} \frac{1}{|\,\hat{\boldsymbol{x}} - \hat{\boldsymbol{y}}\,|} M_1(\hat{\boldsymbol{x}},\hat{\boldsymbol{y}})\boldsymbol{A}(\hat{\boldsymbol{y}})\,\mathrm{d}s(\hat{\boldsymbol{y}}), \tag{2.14}$$

$$\mathcal{M}_2\boldsymbol{A}(\hat{\boldsymbol{x}}) = \int_{\partial B} M_2(\hat{\boldsymbol{x}},\hat{\boldsymbol{y}})\boldsymbol{A}(\hat{\boldsymbol{y}})\,\mathrm{d}s(\hat{\boldsymbol{y}}), \tag{2.15}$$

where for each $\hat{x}, \hat{y} \in \partial B$, $M_1(\hat{x}, \hat{y})$, $M_2(\hat{x}, \hat{y})$ are 3×3 matrices defined by

$$M_1(\hat{x}, \hat{y}) = R(\hat{x}, \hat{y}) J(\hat{y})\, m_1(\boldsymbol{q}(\hat{x}), \boldsymbol{q}(\hat{y})), \tag{2.16}$$

$$M_2(\hat{x}, \hat{y}) = J(\hat{y})\, m_2(\boldsymbol{q}(\hat{x}), \boldsymbol{q}(\hat{y})), \tag{2.17}$$

J is the Jacobian of $\boldsymbol{q}$, and

$$R(\hat{x}, \hat{y}) := \frac{|\, \hat{x} - \hat{y}\,|}{|\, \boldsymbol{q}(\hat{x}) - \boldsymbol{q}(\hat{y})\,|}. \tag{2.18}$$

Thus, using (2.3) and (2.11), we have reformulated the electromagnetic scattering problem described in Section 1 as an integral equation on ∂B. We recall from Section 2.1 that the unique solution $\boldsymbol{w} = \boldsymbol{W} \circ \boldsymbol{q}^{-1}$ of (2.3) is tangential on ∂D. However, in general, $\boldsymbol{W}$ is not tangential on ∂B. Conversely, for a given tangential function $\boldsymbol{A}$ on ∂B, the function $\boldsymbol{A} \circ \boldsymbol{q}^{-1}$ may not be tangential on ∂D. The starting point of the algorithm in this work is the construction of an orthogonal transformation that transforms tangential functions on ∂B to tangential functions on ∂D. More precisely, we construct an orthogonal transformation $\mathcal{F}$ with

$$\boldsymbol{n}(\boldsymbol{q}(\hat{x}))^{\mathrm{T}} \mathcal{F}(\hat{x}) \boldsymbol{A}(\hat{x}) = 0, \quad \text{for all } \boldsymbol{A} \in \underline{T}(\partial B),\ \hat{x} \in \partial B. \tag{2.19}$$

In order to prove spectral accuracy for our algorithm, we require that $\mathcal{F}$ be smooth on ∂B. (Many orthogonal transformations that satisfy (2.19), for example the rotation matrices described in [16], are not smooth and are therefore not appropriate in this setting.)

In our algorithm we define $\mathcal{F}(\hat{x})$ to be the orthogonal transformation that maps $\hat{x}$ to $\boldsymbol{n}(\boldsymbol{q}(\hat{x}))$ by rotation in the plane containing $\hat{x}$ and $\boldsymbol{n}(\boldsymbol{q}(\hat{x}))$.

We choose this transformation in such a way that it rotates any vector $\boldsymbol{y} \in \mathbb{C}^3$ by angle ψ in the counter clockwise direction around the unit vector $\hat{x} \times \boldsymbol{n}(\boldsymbol{q}(\hat{x}))/|\, \hat{x} \times \boldsymbol{n}(\boldsymbol{q}(\hat{x}))\,|$, where $\psi = \cos^{-1}(\hat{x}^{\mathrm{T}} \boldsymbol{n}(\boldsymbol{q}(\hat{x})))$ is the angle between $\hat{x}$ and $\boldsymbol{n}(\boldsymbol{q}(\hat{x}))$. Using the Rodrigues' formula [38, p. 338] and the fact that $|\, \hat{x} \times \boldsymbol{n}(\boldsymbol{q}(\hat{x}))\,| = \sin\psi$, the orthogonal transformation $\mathcal{F}(\hat{x})$ can be written as

$$\mathcal{F}(\hat{x})\boldsymbol{y} = \cos\psi \boldsymbol{y} + [\hat{x} \times \boldsymbol{n}(\boldsymbol{q}(\hat{x}))] \times \boldsymbol{y} + \frac{1}{1+\cos\psi} [[\hat{x} \times \boldsymbol{n}(\boldsymbol{q}(\hat{x}))]^{\mathrm{T}} \boldsymbol{y}][\hat{x} \times \boldsymbol{n}(\boldsymbol{q}(\hat{x}))], \quad \boldsymbol{y} \in \mathbb{C}^3. \tag{2.20}$$

For $\psi \in [0, \pi)$, the rotation (2.20) is well defined and $\mathcal{F}$ is r-times continuously differentiable on ∂B, provided that ∂D is a C^{r+1} surface for $r \geqslant 0$. Throughout the paper we assume that $\psi \neq \pi$, that is,

$$\boldsymbol{n}(\boldsymbol{q}(\hat{x})) \neq -\hat{x}, \quad \text{for all } \hat{x} \in \partial B.$$

(If $\boldsymbol{n}(\boldsymbol{q}(\hat{x})) = -\hat{x}$ for all $\hat{x} \in \partial B$, then the orthogonal transformation is not required because $\boldsymbol{n}(\hat{x}) = \hat{x}$ and hence in this case for $\boldsymbol{A} \in \underline{T}(\partial B)$, we have $\boldsymbol{n}(\boldsymbol{q}(\hat{x}))^{\mathrm{T}} \boldsymbol{A}(\hat{x}) = 0$.) For our analysis, we assume that ∂D is C^{r+1} for some fixed $r \geqslant 0$. The transformation $\mathcal{F}$ is illustrated in Fig. 1. It is convenient to represent $\mathcal{F}(\hat{x})$ by an orthogonal matrix, which we also denote $\mathcal{F}(\hat{x})$. Next we define the action of $\mathcal{F}$ and $\mathcal{F}^{-1}(= \mathcal{F}^{\mathrm{T}})$ on vector fields $\boldsymbol{V}$ and $\boldsymbol{v}$ defined respectively on ∂B and ∂D using the bijective parametrization $\boldsymbol{q}$ as follows:

$$(\mathcal{F} \cdot \boldsymbol{V})(\boldsymbol{x}) = \mathcal{F}(\hat{x}) \boldsymbol{V}(\hat{x}), \quad (\mathcal{F}^{-1} \cdot \boldsymbol{v})(\hat{x}) = \mathcal{F}(\hat{x})^{\mathrm{T}} \boldsymbol{v}(\boldsymbol{q}(\hat{x})), \quad \boldsymbol{x} = \boldsymbol{q}(\hat{x}) \in \partial D, \quad \hat{x} \in \partial B. \tag{2.21}$$

Using Rodrigues' formula, for $\hat{x} \in \partial B$, with $\boldsymbol{y} = \boldsymbol{v}(\boldsymbol{q}(\hat{x}))$, we have

$$(\mathcal{F}^{-1} \cdot \boldsymbol{v})(\hat{x}) = \cos\psi \boldsymbol{y} - [\hat{x} \times \boldsymbol{n}(\boldsymbol{q}(\hat{x}))] \times \boldsymbol{y} + \frac{1}{1+\cos\psi} [[\hat{x} \times \boldsymbol{n}(\boldsymbol{q}(\hat{x}))]^{\mathrm{T}} \boldsymbol{y}][\hat{x} \times \boldsymbol{n}(\boldsymbol{q}(\hat{x}))]. \tag{2.22}$$

Lemma 1. *The C^r orthogonal transformation $\mathcal{F}$ preserves the tangential property between reference and conductor surface*:

(i) *$\mathcal{F} \cdot \boldsymbol{V}$ is tangential on ∂D for any $\boldsymbol{V} \in \underline{T}(\partial B)$ and*
(ii) *$\mathcal{F}^{-1} \cdot \boldsymbol{v}$ is tangential on ∂B for any $\boldsymbol{v} \in \underline{T}(\partial D)$.*

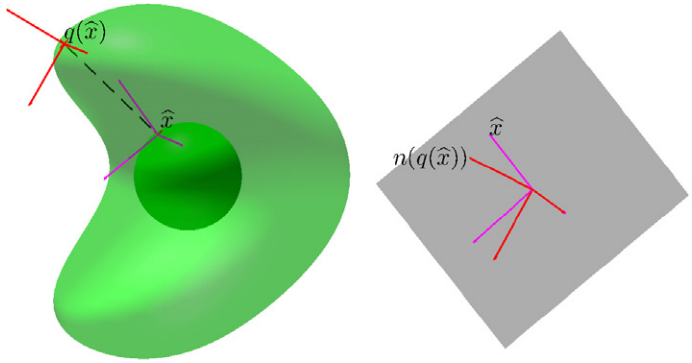

Fig. 1. The unit outward normal to ∂B at $\hat{\boldsymbol{x}}$ and the unit outward normal to ∂D at $\boldsymbol{q}(\hat{\boldsymbol{x}})$ are generally not equal. Hence even if $\boldsymbol{w} = \boldsymbol{W} \circ \boldsymbol{q}^{-1}$ is tangential on ∂D, $\boldsymbol{W}$ need not be tangential on ∂B. The tangential transformation is effected by rotation in the plane containing $\hat{\boldsymbol{x}}$ and $\boldsymbol{n}(\boldsymbol{q}(\hat{\boldsymbol{x}}))$.

Proof.

(i) Let $\boldsymbol{V} \in \underline{T}(\partial B)$ and let $\boldsymbol{x} \in \partial D$ with $\boldsymbol{x} = \boldsymbol{q}(\hat{\boldsymbol{x}})$ for some $\hat{\boldsymbol{x}} \in \partial B$. For brevity we write $\boldsymbol{n} = \boldsymbol{n}(\boldsymbol{q}(\hat{\boldsymbol{x}}))$ and $\boldsymbol{V} = \boldsymbol{V}(\hat{\boldsymbol{x}})$. Using $\cos\psi = \boldsymbol{n}^{\mathrm{T}}\hat{\boldsymbol{x}}$ in (2.20),

$$\boldsymbol{n}^{\mathrm{T}}\mathcal{F}(\hat{\boldsymbol{x}})\boldsymbol{V} = (\boldsymbol{n}^{\mathrm{T}}\hat{\boldsymbol{x}})\boldsymbol{n}^{\mathrm{T}}\boldsymbol{V} + \boldsymbol{n}^{\mathrm{T}}[(\hat{\boldsymbol{x}}\times\boldsymbol{n})\times\boldsymbol{V}] + \frac{1}{1+\boldsymbol{n}^{\mathrm{T}}\hat{\boldsymbol{x}}}[(\hat{\boldsymbol{x}}\times\boldsymbol{n})^{\mathrm{T}}\boldsymbol{V}]\boldsymbol{n}^{\mathrm{T}}(\hat{\boldsymbol{x}}\times\boldsymbol{n}) = (\boldsymbol{n}^{\mathrm{T}}\hat{\boldsymbol{x}})\boldsymbol{n}^{\mathrm{T}}\boldsymbol{V} - \boldsymbol{n}^{\mathrm{T}}[\boldsymbol{V}\times(\hat{\boldsymbol{x}}\times\boldsymbol{n})].$$

Expanding the vector triple product we have

$$\boldsymbol{n}^{\mathrm{T}}\mathcal{F}(\hat{\boldsymbol{x}})\boldsymbol{V} = (\boldsymbol{n}^{\mathrm{T}}\hat{\boldsymbol{x}})\boldsymbol{n}^{\mathrm{T}}\boldsymbol{V} - \boldsymbol{n}^{\mathrm{T}}[(\boldsymbol{V}^{\mathrm{T}}\boldsymbol{n})\hat{\boldsymbol{x}} - \boldsymbol{n}(\boldsymbol{V}^{\mathrm{T}}\hat{\boldsymbol{x}})] = (\boldsymbol{n}^{\mathrm{T}}\hat{\boldsymbol{x}})\boldsymbol{n}^{\mathrm{T}}\boldsymbol{V} - (\boldsymbol{V}^{\mathrm{T}}\boldsymbol{n})\boldsymbol{n}^{\mathrm{T}}\hat{\boldsymbol{x}} + \boldsymbol{V}^{\mathrm{T}}\hat{\boldsymbol{x}} = \boldsymbol{V}^{\mathrm{T}}\hat{\boldsymbol{x}} = 0,$$

where in the last step we have used that $\boldsymbol{V}$ is tangential on ∂B.

(ii) Let $\boldsymbol{v} \in \underline{T}(\partial D)$ and let $\hat{\boldsymbol{x}} \in \partial B$ with $\hat{\boldsymbol{x}} = \boldsymbol{q}^{-1}(\boldsymbol{x})$ for some $\boldsymbol{x} \in \partial D$. An identical argument to above, using (2.22), shows that $\hat{\boldsymbol{x}}^{\mathrm{T}}(\mathcal{F}^{-1}\cdot\boldsymbol{v})(\hat{\boldsymbol{x}}) = 0$. □

We conclude this subsection by defining an additional rotation transformation that is required for spectrally accurate evaluation of the magnetic dipole operator defined in (2.13)–(2.15). The integral operator $\mathcal{M}_2$ has a smooth kernel that can be evaluated with spectral accuracy using spherical polynomial approximation. The weakly singular operator $\mathcal{M}_1$ can be evaluated with similar spectral accuracy by working in a rotated coordinate system in which the weak singularity appears at the north pole $\hat{\boldsymbol{n}} = (0,0,1)^{\mathrm{T}}$. The rotation of the coordinate system for $\hat{\boldsymbol{x}} = \hat{\boldsymbol{p}}(\theta,\phi)$ is induced by the orthogonal matrix $T_{\hat{\boldsymbol{x}}}$, which maps $\hat{\boldsymbol{x}}$ to $\hat{\boldsymbol{n}}$ and is given by

$$T_{\hat{\boldsymbol{x}}} := \mathcal{R}_z(\phi)\mathcal{R}_y(-\theta)\mathcal{R}_z(-\phi), \tag{2.23}$$

where

$$\mathcal{R}_y(\psi) := \begin{pmatrix} \cos\psi & 0 & \sin\psi \\ 0 & 1 & 0 \\ -\sin\psi & 0 & \cos\psi \end{pmatrix}, \qquad \mathcal{R}_z(\psi) = \begin{pmatrix} \cos\psi & -\sin\psi & 0 \\ \sin\psi & \cos\psi & 0 \\ 0 & 0 & 1 \end{pmatrix}. \tag{2.24}$$

Since $T_{\hat{\boldsymbol{x}}}$ is an orthogonal matrix we have, for $\hat{\boldsymbol{x}}, \hat{\boldsymbol{z}} \in \partial B$ and $\hat{\boldsymbol{y}} = T_{\hat{\boldsymbol{x}}}^{-1}\hat{\boldsymbol{z}}$,

$$|\,\hat{\boldsymbol{x}} - \hat{\boldsymbol{y}}\,| = |\,T_{\hat{\boldsymbol{x}}}^{-1}(\hat{\boldsymbol{n}} - \hat{\boldsymbol{z}})\,| = |\,\hat{\boldsymbol{n}} - \hat{\boldsymbol{z}}\,|\,. \tag{2.25}$$

Using the linear transformation

$$\mathcal{T}_{\hat{\boldsymbol{x}}}\boldsymbol{A}(\hat{\boldsymbol{z}}) := \boldsymbol{A}(T_{\hat{\boldsymbol{x}}}^{-1}\hat{\boldsymbol{z}}), \qquad \hat{\boldsymbol{z}} \in \partial B, \qquad \boldsymbol{A} \in \underline{C}(\partial B), \tag{2.26}$$

and its bivariate analogue

$$\mathcal{T}_{\hat{\boldsymbol{x}}}\boldsymbol{A}(\hat{\boldsymbol{z}}_1,\hat{\boldsymbol{z}}_2) := \boldsymbol{A}(T_{\hat{\boldsymbol{x}}}^{-1}\hat{\boldsymbol{z}}_1, T_{\hat{\boldsymbol{x}}}^{-1}\hat{\boldsymbol{z}}_2), \qquad \hat{\boldsymbol{z}}_1,\hat{\boldsymbol{z}}_2 \in \partial B, \qquad \boldsymbol{A} \in \underline{C}(\partial B \times \partial B), \tag{2.27}$$

we write (2.14) as

$$\mathcal{M}_1 \boldsymbol{A}(\hat{\boldsymbol{x}}) = \int_{\partial B} \frac{1}{|\,\hat{\boldsymbol{n}} - \hat{\boldsymbol{z}}\,|}\, \mathcal{T}_{\hat{\boldsymbol{x}}} M_1(\hat{\boldsymbol{n}}, \hat{\boldsymbol{z}})\, \mathcal{T}_{\hat{\boldsymbol{x}}} \boldsymbol{A}(\hat{\boldsymbol{z}})\, \mathrm{d}s(\hat{\boldsymbol{z}}), \quad \boldsymbol{A} \in \underline{C}(\partial B). \tag{2.28}$$

Here we have used the invariance of the surface measure on ∂B. Evaluating the operator using (2.28), where the integrand is expressed in the rotated coordinate system, facilitates the spectrally accurate approximation in Section 3.2.

3. A fully discrete high-order spectral algorithm

3.1. Ansatz spaces

The crucial component of our algorithm is the development of a suitable sequence of ansatz spaces for the Galerkin scheme to approximate electromagnetic fields that are tangential on ∂D.

We have the following requirements from each ansatz space: (i) spectrally accurate approximation of tangential functions on the parametrized surface (that is, for any $\boldsymbol{f} \in \underline{T}^r(\partial D)$ the ansatz space should contain a function $\boldsymbol{G}$ with $\|\boldsymbol{f} \circ \boldsymbol{q} - \boldsymbol{G}\|_{\infty,\partial B} \leqslant cN^{-r}$, where N represents the dimension of the ansatz space); (ii) $\boldsymbol{G} \circ \boldsymbol{q}^{-1}$ is tangential on ∂D for all functions $\boldsymbol{G}$ in the ansatz space; (iii) the ansatz space has an orthonormal basis, and each member of the basis has a separable form similar to that for the spherical harmonics. The latter property allows for fast transformations using the orthonormal basis. We note that the orthonormality here (in the ansatz spaces) is with respect to the L_2 inner product

$$(\boldsymbol{G}, \boldsymbol{H}) = \mathcal{I}(\overline{\boldsymbol{H}}^{\mathrm{T}} \boldsymbol{G}) = \int_{\partial B} \overline{\boldsymbol{H}}^{\mathrm{T}}(\hat{\boldsymbol{x}}) \boldsymbol{G}(\hat{\boldsymbol{x}})\, \mathrm{d}s(\hat{\boldsymbol{x}}). \tag{3.1}$$

We proceed in this section by introducing such a basis, and using the basis to define the approximation space. For $\hat{\boldsymbol{x}} \in \partial B$, let

$$\boldsymbol{Z}^{(1)}_{l,j}(\hat{\boldsymbol{x}}) = \mathcal{F}(\hat{\boldsymbol{x}}) \boldsymbol{Y}^{(1)}_{l,j}(\hat{\boldsymbol{x}}), \qquad \boldsymbol{Y}^{(1)}_{l,j}(\hat{\boldsymbol{x}}) = \frac{1}{\sqrt{l(l+1)}} \mathbf{Grad}\, Y_{l,j}(\hat{\boldsymbol{x}}), \tag{3.2}$$

$$\boldsymbol{Z}^{(2)}_{l,j}(\hat{\boldsymbol{x}}) = \mathcal{F}(\hat{\boldsymbol{x}}) \boldsymbol{Y}^{(2)}_{l,j}(\hat{\boldsymbol{x}}), \qquad \boldsymbol{Y}^{(2)}_{l,j}(\hat{\boldsymbol{x}}) = \hat{\boldsymbol{x}} \times \frac{1}{\sqrt{l(l+1)}} \mathbf{Grad}\, Y_{l,j}(\hat{\boldsymbol{x}}), \tag{3.3}$$

where **Grad** is the surface gradient [9, p. 167]. We choose the ansatz space for our algorithm to be

$$\underline{\mathbb{T}}_n = \mathrm{span}\left\{ \boldsymbol{Z}^{(\tilde{k})}_{l,j} : 1 \leqslant l \leqslant n,\ |\, j\,| \leqslant l, \tilde{k} = 1, 2 \right\}.$$

Next we show that the space $\underline{\mathbb{T}}_n$ spanned by non-polynomial functions $\boldsymbol{Z}^{(1)}_{l,j}$, $\boldsymbol{Z}^{(2)}_{l,j}$ on ∂B satisfies the three requirements above.

Theorem 2. *Let $\boldsymbol{f} \in \underline{T}^r(\partial D)$. Then,*

(i) *For $n > 3$ there exists $\boldsymbol{F}_n \in \underline{\mathbb{T}}_n$ and a constant c_r independent of n such that*

$$\|\boldsymbol{F}_n - \boldsymbol{f} \circ \boldsymbol{q}\|_{j,\infty,\partial B} \leqslant c_r \frac{1}{n^{r-j}} \|\boldsymbol{f} \circ \boldsymbol{q}\|_{r,\infty,\partial B}, \qquad 0 \leqslant j \leqslant r. \tag{3.4}$$

(ii) $\boldsymbol{Z}^{(\tilde{k})}_{l,j} \circ \boldsymbol{q}^{-1} \in \underline{T}(\partial D)$ *for* $1 \leqslant l \leqslant n, |\, j\,| \leqslant l, \tilde{k} = 1, 2$.

(iii) *For* $1 \leqslant l, l' \leqslant n,\ |\, j\,| \leqslant l,\ |\, j'\,| \leqslant l',\ \tilde{k}, k' = 1, 2,$

$$\left(\boldsymbol{Z}^{(\tilde{k})}_{l,j}, \boldsymbol{Z}^{(k')}_{l',j'} \right) = \left(\boldsymbol{Y}^{(\tilde{k})}_{l,j}, \boldsymbol{Y}^{(k')}_{l',j'} \right) = \delta_{ll'} \delta_{jj'} \delta_{\tilde{k}k'}. \tag{3.5}$$

Proof

(i) Let $\underline{\mathbb{P}}_n$ denote the space of vector spherical polynomials, whose Euclidean components are spherical polynomials of degree not greater than $n > 3$. For $\boldsymbol{f} \in \underline{T}^r(\partial D)$, using (2.21), let $\boldsymbol{\Psi} = \mathcal{F}^{-1} \cdot \boldsymbol{f}$. Using Lemma 1, $\boldsymbol{\Psi} \in T(\partial B)$ and is r-times continuously differentiable on ∂B. Hence using [17, (A.1), p. 53] there exists $\boldsymbol{\Psi}_{n-3} \in \underline{\mathbb{P}}_{n-3}$ such that

$$\|\boldsymbol{\Psi}_{n-3}-\boldsymbol{\Psi}\|_{j,\infty,\partial B} \leqslant c_r \frac{1}{(n-3)^{r-j}} \|\boldsymbol{\Psi}\|_{r,\infty,\partial B}, \qquad 0 \leqslant j \leqslant r. \tag{3.6}$$

Let $\mathcal{P}$ denote the tangential projection $I-\hat{\boldsymbol{x}}\hat{\boldsymbol{x}}^{\mathrm{T}}$. Note that $\boldsymbol{\Psi}_{n-3}$ may not be tangential to ∂B, but $\mathcal{P}\boldsymbol{\Psi}_{n-3} \in \underline{\mathbb{P}}_{n-1}$ is tangential to ∂B. Thus $\mathcal{F}\mathcal{P}\boldsymbol{\Psi}_{n-3} \in \underline{\mathbb{T}}_n$ [14, p. 325]. Let $\boldsymbol{F} := \mathcal{F}\cdot\boldsymbol{\Psi} = \boldsymbol{f}\circ\boldsymbol{q}$ and $\boldsymbol{F}_n := \mathcal{F}\cdot\mathcal{P}\boldsymbol{\Psi}_n$. Then, since $\boldsymbol{\Psi}$ is tangential on ∂B, $\mathcal{P}\boldsymbol{\Psi}=\boldsymbol{\Psi}$, and using (3.6),

$$\begin{aligned}\|\boldsymbol{F}_n-\boldsymbol{f}\circ\boldsymbol{q}\|_{j,\infty,\partial B} &= \|\boldsymbol{F}_n-\boldsymbol{F}\|_{j,\infty,\partial B} \leqslant \|\mathcal{F}\|_{j,\infty,\partial B}\|\mathcal{P}\|_{j,\infty,\partial B}\|\boldsymbol{\Psi}_{n-3}-\boldsymbol{\Psi}\|_{j,\infty,\partial B} \leqslant c_r\frac{1}{(n-3)^{r-j}}\|\boldsymbol{\Psi}\|_{r,\infty,\partial B}\\ &\leqslant c_r\frac{1}{n^{r-j}}\|\boldsymbol{f}\circ\boldsymbol{q}\|_{r,\infty,\partial B}.\end{aligned}$$

(ii) The result follows from Lemma 1 because $\boldsymbol{Y}_{l,j}^{(1)}$ and $\boldsymbol{Y}_{l,j}^{(2)}$ are tangential on ∂B.

(iii) Using (3.1)–(3.3),

$$(\boldsymbol{Z}_{l,j}^{(\tilde{k})}, \boldsymbol{Z}_{l',j'}^{(k')}) = \int_{\partial B} \overline{\boldsymbol{Y}_{l',j'}^{(k')}(\hat{\boldsymbol{y}})}\mathcal{F}(\hat{\boldsymbol{y}})^{\mathrm{T}}\mathcal{F}(\hat{\boldsymbol{y}})\boldsymbol{Y}_{l,j}^{(\tilde{k})}(\hat{\boldsymbol{y}})\,\mathrm{d}s(\hat{\boldsymbol{y}}) = \int_{\partial B} \overline{\boldsymbol{Y}_{l',j'}^{(k')}(\hat{\boldsymbol{y}})}\boldsymbol{Y}_{l,j}^{(\tilde{k})}(\hat{\boldsymbol{y}})\,\mathrm{d}s(\hat{\boldsymbol{y}}).$$

The result follows from the orthonormality of the vector spherical harmonics $\boldsymbol{Y}_{l,j}^{(\tilde{k})}$ [9, Theorem 6.23, p. 178]. □

To evaluate the Galerkin inner product integrals (3.1) in our fully discrete Galerkin scheme, we approximate the integrals numerically using the Gauss-rectangle quadrature rule given by the following formula (for a continuous scalar valued function G on ∂B):

$$\int_{\partial B} G(\hat{\boldsymbol{x}})\,\mathrm{d}s(\hat{\boldsymbol{x}}) \approx Q_n(G) = \sum_{r=0}^{2n+3}\sum_{s=1}^{n+2} \mu_r^{n+1} v_s^{n+1} G(\hat{\boldsymbol{z}}_{rs}^{n+1}), \tag{3.7}$$

where, using (1.6), $\hat{\boldsymbol{z}}_{rs}^{n+1} = \boldsymbol{p}(\theta_s^{n+1}, \phi_r^{n+1})$, $\theta_s^{n+1} = \cos^{-1} z_s$, z_s are the zeros of the Legendre polynomial of degree $n+2$, v_s^{n+1} are the corresponding Gauss–Legendre weights ($s=1,\ldots,n+2$), and

$$\mu_r^{n+1} = \frac{\pi}{n+2}, \quad \phi_r^{n+1} = \frac{r\pi}{n+2}, \qquad r=0,\ldots,2n+3. \tag{3.8}$$

Since the quadrature (3.7) is exact for spherical polynomials of degree at most $2n+2$, using Theorem 2(iii), we obtain an induced discrete inner product

$$(\boldsymbol{G},\boldsymbol{H})_n = Q_n(\overline{\boldsymbol{H}}^{\mathrm{T}}\boldsymbol{G}) = \sum_{r=0}^{2n+3}\sum_{s=1}^{n+2} \mu_r^{n+1} v_s^{n+1} \overline{\boldsymbol{H}(\hat{\boldsymbol{z}}_{rs}^{n+1})}^{\mathrm{T}} \boldsymbol{G}(\hat{\boldsymbol{z}}_{rs}^{n+1}), \quad \boldsymbol{G},\boldsymbol{H} \in \underline{T}(\partial B). \tag{3.9}$$

It follows (using also Theorem 2(iii)) that

$$(\boldsymbol{G},\boldsymbol{H}) = (\boldsymbol{G},\boldsymbol{H})_n, \quad \boldsymbol{G},\boldsymbol{H} \in \underline{\mathbb{T}}_n. \tag{3.10}$$

Using the non-polynomial basis (3.2), (3.3) and (3.10), we define a fully discrete orthogonal projection operator

$$\underline{\mathcal{O}}_n\boldsymbol{A} = \sum_{l=0}^{n}\sum_{|j|\leqslant l}\sum_{\tilde{k}=1}^{2} (\boldsymbol{A}, \boldsymbol{Z}_{l,j}^{(\tilde{k})})_n\, \boldsymbol{Z}_{l,j}^{(\tilde{k})}, \qquad \boldsymbol{A}\circ\boldsymbol{q}^{-1} \in \underline{T}(\partial D). \tag{3.11}$$

Using (3.10), clearly $\underline{\mathcal{O}}_n\boldsymbol{A}=\boldsymbol{A}$ for all $\boldsymbol{A}\in\underline{\mathbb{T}}_n$. In [17] a similar operator to $\underline{\mathcal{O}}_n$ that involves componentwise harmonics (which are not, in general, tangential) was shown to retain the $\mathcal{O}(\sqrt{n})$ Lebesgue constant bound of its continuous counterpart (that is, the discrete operator modified by replacing the discrete inner product by the L_2 inner product). Such an optimal $\mathcal{O}(\sqrt{n})$ bound in [17] was obtained using results in [31,32]. We conjecture that

$$\|\underline{\mathcal{O}}_n\|_{\infty,\partial B} \leqslant cn^{\alpha}, \quad \alpha<1. \tag{3.12}$$

A complete proof of this result similar to the analyses in [31,32] is beyond the scope of this paper. (We have observed the bound (3.12) numerically for various values of $n \leqslant 200$.)

We complete this subsection by giving a convenient separable representation of the basis functions. Using (1.6), (2.10), (3.2) and (3.3), for $\tilde{k} = 1, 2$, we have the following representation [18]

$$\boldsymbol{Z}_{l,j}^{(\tilde{k})}(\hat{\boldsymbol{x}}) = \mathcal{F}(\hat{\boldsymbol{x}}) \sum_{t=1}^{2} \alpha_{l,j}^{(\tilde{k},t)}(\theta) \mathrm{e}^{\mathrm{i}j\phi} \boldsymbol{v}^{(t)}(\theta,\phi), \qquad \hat{\boldsymbol{x}} \in \partial B, \tag{3.13}$$

where, denoting the normalizing coefficient in (2.10) by c_l^j,

$$\boldsymbol{v}^{(1)}(\theta,\phi) = (\cos\theta\cos\phi, \cos\theta\sin\phi, -\sin\theta)^{\mathrm{T}}, \ \boldsymbol{v}^{(2)}(\theta,\phi) = (-\sin\phi, \cos\phi, 0)^{\mathrm{T}},$$
$$\alpha_{l,j}^{(1,1)}(\theta) = \alpha_{l,j}^{(2,2)}(\theta) = c_l^j P_l^{|j|'}(\cos\theta)/\sqrt{l(l+1)},$$
$$\alpha_{l,j}^{(1,2)}(\theta) = -\alpha_{l,j}^{(2,1)}(\theta) = c_l^j (ij/\sin\theta) P_l^{|j|}(\cos\theta)/\sqrt{l(l+1)}.$$

3.2. A fully discrete Galerkin method

We have introduced all of the necessary ingredients for describing a semi-discrete spectrally accurate Galerkin algorithm, which is not computer implementable. In order to define a *fully* discrete algorithm for (2.12), we additionally require quadrature discretization of the parametrized magnetic dipole operator (2.13)–(2.18). We use the spectrally accurate approximation described in detail in [17,18] to approximate $\mathcal{M}$ by $\mathcal{M}_{n'}$ of the form

$$\mathcal{M}_{n'}\boldsymbol{A}(\hat{\boldsymbol{x}}) = \mathcal{M}_{1,n'}\boldsymbol{A}(\hat{\boldsymbol{x}}) + \mathcal{M}_{2,n'}\boldsymbol{A}(\hat{\boldsymbol{x}}), \tag{3.14}$$

with [18, Eq. (3.14)]

$$\mathcal{M}_{1,n'}\boldsymbol{A}(\hat{\boldsymbol{x}}) = \sum_{r'=0}^{2n'+1} \sum_{s'=1}^{n'+1} \mu_{r'}^{n'} v_{s'}^{n'} \alpha_{s'}^{n'} \mathcal{T}_{\hat{\boldsymbol{x}}} M_1(\hat{\boldsymbol{n}}, \hat{\boldsymbol{z}}_{r's'}^{n'}) \, \mathcal{T}_{\hat{\boldsymbol{x}}} \boldsymbol{A}(\hat{\boldsymbol{z}}_{r's'}^{n'}), \tag{3.15}$$

where $\alpha_{s'}^{n'} = \sum_{l=0}^{n'} P_l(\cos\theta_{s'}^{n'})$, and we have used $\hat{\boldsymbol{n}} \cdot \hat{\boldsymbol{z}}_{r's'}^{n'} = \cos\theta_{s'}^{n'}$, and [18, Eq. (3.17)]

$$\mathcal{M}_{2,n'}\boldsymbol{A}(\hat{\boldsymbol{x}}) = \sum_{r'=0}^{2n'+1} \sum_{s'=1}^{n'+1} \mu_{r'}^{n'} v_{s'}^{n'} \mathcal{T}_{\hat{\boldsymbol{x}}} M_2(\hat{\boldsymbol{n}}, \hat{\boldsymbol{z}}_{r's'}^{n'}) \, \mathcal{T}_{\hat{\boldsymbol{x}}} \boldsymbol{A}(\hat{\boldsymbol{z}}_{r's'}^{n'}). \tag{3.16}$$

A small modification to the proof of [17, Theorem 1] shows that, by choosing $n' = an + 1$ for some fixed constant $a > 1$, and $n' - n \geqslant 3$ we obtain the following spectral accuracy in the magnetic dipole operator approximation: if the conductor surface is smooth then for any $s \in \mathbb{N}$, there exists $c_s > 0$, independent of n and n', such that

$$\|(\mathcal{M} - \mathcal{M}_{n'})\boldsymbol{P}_n\|_{\infty,\partial B} \leqslant c_s \frac{1}{n^s} \|\boldsymbol{P}_n\|_{\infty,\partial B} \quad \text{for all } \boldsymbol{P}_n \in \underline{\mathbb{T}}_n. \tag{3.17}$$

In the computational algorithm described below, the density function of the fully discrete magnetic dipole operator is always a function in $\underline{\mathbb{T}}_n$. For computations in Section 5 we set $n' = 2n + 1$.

We are now ready to describe the complete algorithm to solve (2.12), using the various spectrally accurate approximations described above. Our fully discrete scheme for (2.12) is: compute $\boldsymbol{W}_n \in \underline{\mathbb{T}}_n$ such that

$$\boldsymbol{W}_n + \underline{\mathcal{O}}_n \mathcal{M}_{n'} \boldsymbol{W}_n = \underline{\mathcal{O}}_n \boldsymbol{f}. \tag{3.18}$$

Since $\boldsymbol{W}_n \in \underline{\mathbb{T}}_n$ can be written as

$$\boldsymbol{W}_n(\hat{\boldsymbol{x}}) = \sum_{l=1}^{n} \sum_{|j| \leqslant l} \sum_{\tilde{k}=1}^{2} \mathrm{w}_{lj\tilde{k}} \boldsymbol{Z}_{l,j}^{(\tilde{k})}(\hat{\boldsymbol{x}}), \quad \hat{\boldsymbol{x}} \in \partial B, \tag{3.19}$$

the operator equation (3.18) is equivalent to the requirement that the coefficients $\mathrm{w}_{lj\tilde{k}}$ solve the fully discrete Galerkin system

$$(\boldsymbol{W}_n, \boldsymbol{Z}_{l',j'}^{(k')})_n + (\mathcal{M}_{n'}\boldsymbol{W}_n, \boldsymbol{Z}_{l',j'}^{(k')})_n = (\boldsymbol{F}, \boldsymbol{Z}_{l',j'}^{(k')})_n, \quad l' = 1, \ldots, n, \ |j'| \leqslant l, \ k' = 1, 2. \tag{3.20}$$

In matrix form, $\mathrm{w} = (\mathrm{w}_{l\tilde{j}\tilde{k}})$ satisfies

$$(\mathrm{I} + \mathrm{M})\mathrm{w} = \mathrm{f}, \tag{3.21}$$

where $\mathrm{w} = (\mathrm{w}_{l\tilde{j}\tilde{k}})$, and

$$\mathrm{M}_{l'j'k',l\tilde{j}\tilde{k}} = (\mathcal{M}_{n'}\boldsymbol{Z}^{(\tilde{k})}_{l,\tilde{j}}, \boldsymbol{Z}^{(k')}_{l',j'})_n, \qquad \mathrm{I}_{l'j'k',l\tilde{j}\tilde{k}} = \delta_{ll'}\delta_{jj'}\delta_{\tilde{k}k'}, \qquad \mathrm{f}_{l'j'k'} = (\boldsymbol{F}, \boldsymbol{Z}^{(k')}_{l',j'})_n. \tag{3.22}$$

Our approximation to the solution $\boldsymbol{w}$ of (2.3) is then

$$\boldsymbol{w}_n(\boldsymbol{x}) = \boldsymbol{W}_n \circ \boldsymbol{q}^{-1}(\boldsymbol{x}), \quad \boldsymbol{x} \in \partial D. \tag{3.23}$$

Similar to Theorem 3 in [17], we have the following spectrally accurate convergence result for smooth surfaces.

Theorem 3. *Let $\boldsymbol{w}$ be the unique solution of (2.3). Let $n, n' \in \mathbb{N}$ be sufficiently large that $n' = an + 1$ for some fixed $a > 1$ and $n' - n > 3$. Let $\boldsymbol{w}_n$ be the fully discrete approximation in (3.23). Let (3.12) hold. Then for any $q \in \mathbb{N}$ there exists $c_q > 0$, independent of n and n', such that*

$$\|\boldsymbol{w} - \boldsymbol{w}_n\|_{\infty,\partial D} \leqslant c_q \frac{1}{n^q} \|\boldsymbol{w}\|_{q+1,\infty,\partial D}.$$

Proof. The proof follows from arguments identical to the proof of Theorem 3 in [17] using (3.17) and the spectrally accurate approximation result (i) in Theorem 2 (with $j = 0$). □

3.3. Implementation

In this section, we describe an efficient way to set up the $N \times N$ electromagnetic scattering matrix M in (3.21), (3.22), where $N = 2(n+1)^2 - 2$. We remark that for the algorithms in [17,18], which include non-tangential basis functions, the dimension of the scattering matrix is more than $1.5N$, showing the marked advantage in the current algorithm, which has the same accuracy but a reduction by at least 10,000 in the dimension of the dense complex system for the case $n \geqslant 100$.

We show that M can be computed in $\mathrm{O}(N^{2.5})$ operations. This complexity can be reduced further by making use of fast transforms.

Using (3.15), (3.16), [18, Eq. (3.26)], and (3.13) we get

$$\begin{aligned}
\mathrm{M}_{l'j'k',l\tilde{j}\tilde{k}} = {} & \sum_{r=0}^{2n+3} \sum_{s=1}^{n+2} \mu_r^{n+1} v_s^{n+1} \sum_{r'=0}^{2n'+1} \sum_{s'=1}^{n'+1} \mu_{r'}^{n'} v_{s'}^{n'} \\
& \times \sum_{t'=1}^{2} \alpha^{(k',t')}_{l',j'}(\theta_s^{n+1}) \mathrm{e}^{-\mathrm{i}j'\phi_r^{n+1}} \boldsymbol{v}^{(t')}(\theta_s^{n+1}, \phi_r^{n+1})^{\mathrm{T}} \mathcal{F}^{\mathrm{T}}(\hat{\boldsymbol{x}}_{rs}) \big[\alpha_{s'}^{n'} M_1(\hat{\boldsymbol{x}}_{rs}, \hat{\boldsymbol{y}}_{rs}^{r's'}) + M_2(\hat{\boldsymbol{x}}_{rs}, \hat{\boldsymbol{y}}_{rs}^{r's'})\big] \mathcal{F}(\boldsymbol{y}_{rs}^{r's'}) \\
& \times \sum_{|\tilde{j}| \leqslant l} F_{sl\tilde{j}j} \mathrm{e}^{\mathrm{i}(j-\tilde{j})\phi_r^{n+1}} \sum_{t=1}^{2} \alpha^{(\tilde{k},t)}_{l,\tilde{j}}(\theta_{s'}^{n'}) \mathrm{e}^{\mathrm{i}\tilde{j}\phi_{r'}^{n'}} T^{-1}_{\hat{\boldsymbol{x}}_{rs}} \boldsymbol{v}^{(t)}(\theta_{s'}^{n'}, \phi_{r'}^{n'}),
\end{aligned}$$

where we have written $\boldsymbol{y}_{rs}^{r's'} = T^{-1}_{\hat{\boldsymbol{x}}_{rs}} \hat{\boldsymbol{z}}_{r's'}$ and introduced $F_{sl\tilde{j}j}$ from [18, Eq. (3.26)].

The matrix M, which has $\mathrm{O}(N^2) = \mathrm{O}(n^4)$ entries, can be computed by successively computing the following arrays. Each array is a sum with $\mathrm{O}(n)$ terms and depends on four labels (ignoring $\tilde{k}$ and k'). Thus M can be computed in $\mathrm{O}(n^5) = \mathrm{O}(N^{2.5})$ operations.

$$\mathrm{E}_{srs'\tilde{j}t} = \sum_{r'=0}^{2n'+1} \mu_{r'}^{n'} \mathrm{e}^{\mathrm{i}\tilde{j}\phi_{r'}^{n'}} \mathcal{F}^{\mathrm{T}}(\hat{\boldsymbol{x}}_{rs}) \big[\alpha_{s'}^{n'} M_1(\hat{\boldsymbol{x}}_{rs}, \hat{\boldsymbol{y}}_{rs}^{r's'}) + M_2(\hat{\boldsymbol{x}}_{rs}, \hat{\boldsymbol{y}}_{rs}^{r's'})\big] \mathcal{F}(\boldsymbol{y}_{rs}^{r's'}) T^{-1}_{\hat{\boldsymbol{x}}_{rs}} \boldsymbol{v}^{(t)}(\theta_{s'}^{n'}, \phi_{r'}^{n'}),$$

$$\mathrm{D}_{srl\tilde{j}\tilde{k}} = \sum_{s'=1}^{n'+1} \sum_{t=1}^{2} v_{s'}^{n'} \alpha^{(\tilde{k},t)}_{l,\tilde{j}}(\theta_{s'}^{n'}) \mathrm{E}_{srs'\tilde{j}t}, \quad \mathrm{C}_{srl\tilde{j}\tilde{k}} = \sum_{|\tilde{j}| \leqslant l} F_{sl\tilde{j}j} \mathrm{e}^{\mathrm{i}(j-\tilde{j})\phi_r^{n+1}} \mathrm{D}_{srl\tilde{j}\tilde{k}},$$

$$\mathrm{B}_{sj't'1j\tilde{k}} = \sum_{r=0}^{2n+3} \mu_r^{n+1} \mathrm{e}^{-\mathrm{i}j'\phi_r^{n+1}} \boldsymbol{v}^{(t')}(\theta_s^{n+1}, \phi_s^{n+1})^{\mathrm{T}} \mathrm{C}_{srlj\tilde{k}},$$

$$\mathrm{M}_{l'j'k',lj\tilde{k}} = \sum_{s=1}^{n+2} \sum_{t'=1}^{2} v_s^{n+1} \alpha_{l',j'}^{(k',t')}(\theta_s^{n+1}) \mathrm{B}_{sj't'1j\tilde{k}}.$$

Once E has been used to compute D, it is discarded. Similarly, D is discarded after it has been used to compute C, and so on. The fast Fourier transform (FFT) can be used to speed up the computation of the arrays above, and for calculating f and F in (3.22) and [18, Eq. (3.26)], respectively.

4. Exterior field and far field computations

Using (2.5) and (3.23), the far field corresponding to $\boldsymbol{w}_n = \boldsymbol{W}_n \circ \boldsymbol{q}^{-1}$ is given by

$$\widehat{\mathcal{M}}\boldsymbol{W}_n(\hat{\boldsymbol{x}}) := \frac{\mathrm{i}k}{4\pi} \int_{\partial D} \mathrm{e}^{-\mathrm{i}k\hat{\boldsymbol{x}}\cdot\boldsymbol{y}} \hat{\boldsymbol{x}} \times \boldsymbol{w}_n(\boldsymbol{y})\, \mathrm{d}s(\boldsymbol{y}) = \int_{\partial B} \widehat{M}_{\hat{\boldsymbol{x}}}(\hat{\boldsymbol{y}}) \boldsymbol{W}_n(\hat{\boldsymbol{y}})\, \mathrm{d}s(\hat{\boldsymbol{y}}) \quad \hat{\boldsymbol{x}} \in \partial B,$$

where

$$\widehat{M}_{\hat{\boldsymbol{x}}}(\hat{\boldsymbol{y}}) \boldsymbol{W}_n(\hat{\boldsymbol{y}}) = \frac{\mathrm{i}k}{4\pi} J(\hat{\boldsymbol{y}}) \mathrm{e}^{-\mathrm{i}k\hat{\boldsymbol{x}}\cdot\boldsymbol{q}(\hat{\boldsymbol{y}})} \hat{\boldsymbol{x}} \times \boldsymbol{W}_n(\hat{\boldsymbol{y}}), \quad \hat{\boldsymbol{y}} \in \partial B.$$

Hence the representation (3.19) yields

$$\widehat{\mathcal{M}}\boldsymbol{W}_n(\hat{\boldsymbol{x}}) = \sum_{l=1}^{n} \sum_{|j|\leqslant n} \sum_{\tilde{k}=1}^{2} \mathrm{w}_{lj\tilde{k}} \widehat{\mathcal{M}} \boldsymbol{Z}_{l,j}^{(\tilde{k})}(\hat{\boldsymbol{x}}).$$

We compute a spectrally accurate approximation $\boldsymbol{E}_{n,\infty}$ to $\boldsymbol{E}_\infty$ using the approximation to $\widehat{\mathcal{M}}$ described in [18, Section 4.1], which we denote $\widehat{\mathcal{M}}_n$. Our approximation is then

$$\boldsymbol{E}_{n,\infty}(\hat{\boldsymbol{x}}) = \sum_{l=1}^{n} \sum_{|j|\leqslant n} \sum_{\tilde{k}=1}^{2} \mathrm{w}_{lj\tilde{k}} \widehat{\mathcal{M}}_n \boldsymbol{Z}_{l,j}^{(\tilde{k})}(\hat{\boldsymbol{x}}).$$

The quantities $\widehat{\mathcal{M}}_n \boldsymbol{Z}_{l,j}^{(\tilde{k})}(\hat{\boldsymbol{x}})$ do not depend on $\boldsymbol{W}_n$ and can be precomputed independently.

A similar approach yields a spectrally accurate approximation $\boldsymbol{E}_n$ to the exterior field $\boldsymbol{E}$. From (2.1), the exterior field corresponding to $\boldsymbol{w}_n = \boldsymbol{W}_n \circ \boldsymbol{q}^{-1}$ is given by

$$\widetilde{\mathcal{M}}\boldsymbol{W}_n(\boldsymbol{x}) := \mathbf{curl} \int_{\partial D} \Phi(\boldsymbol{x}, \boldsymbol{y}) \boldsymbol{w}(\boldsymbol{y})\, \mathrm{d}s(\boldsymbol{y}) = \int_{\partial B} \widetilde{M}_{\boldsymbol{x}}(\hat{\boldsymbol{y}}) \boldsymbol{W}_n(\hat{\boldsymbol{y}})\, \mathrm{d}s(\hat{\boldsymbol{y}}), \quad \boldsymbol{x} \in \mathbb{R}^3 \setminus \overline{D},$$

where

$$\widetilde{M}_{\boldsymbol{x}} \boldsymbol{W}_n(\hat{\boldsymbol{y}}) = J(\hat{\boldsymbol{y}})\, \mathbf{curl}_{\boldsymbol{x}} \{\Phi(\boldsymbol{x}, \boldsymbol{q}(\hat{\boldsymbol{y}})) \boldsymbol{W}_n(\hat{\boldsymbol{y}})\}.$$

Using the approximation $\widetilde{\mathcal{M}}_n$ to $\widetilde{\mathcal{M}}$ described in [18, Section 4.2] and (3.19), our approximation is then

$$\boldsymbol{E}_n(\hat{\boldsymbol{x}}) = \sum_{l=1}^{n} \sum_{|j|\leqslant n} \sum_{\tilde{k}=1}^{2} \mathrm{w}_{lj\tilde{k}} \widetilde{\mathcal{M}}_n \boldsymbol{Z}_{l,j}^{(\tilde{k})}(\hat{\boldsymbol{x}}).$$

As in the far field computations, the quantities $\widetilde{\mathcal{M}}_n \boldsymbol{Z}_{l,j}^{(\tilde{k})}(\hat{\boldsymbol{x}})$ do not depend on $\boldsymbol{W}_n$ and can be precomputed independently.

5. Numerical experiments

We compute approximations to the surface current, exterior field, and monostatic and bistatic RCS by solving the electromagnetic scattering problem (1.2)–(1.4) at various frequencies. The boundary condition (1.4) is induced by the plane wave (1.5) with incident unit vector direction $\hat{\boldsymbol{d}}_0 = -\boldsymbol{p}(\theta, \phi)$, given by (1.6) and with

polarization $\hat{\boldsymbol{p}}_0$ that is either horizontal (H, where $\hat{\boldsymbol{p}}_0 = (-\sin\phi, \cos\phi, 0)^{\mathrm{T}}$) or vertical (V, where $\hat{\boldsymbol{p}}_0 = (\cos\theta\cos\phi, \cos\theta\sin\phi, -\sin\theta)^{\mathrm{T}}$) [35, pp. 8–9].

In the case of spherical scatterers, the exact scattered field is given analytically by the Mie series. Using the Mie series we are able compute exact errors in our computed approximation to the far field. For non-spherical scatterers the exact scattered field is not known, in general. To validate our algorithm for non-spherical scatterers we simulate the electric field induced by an off-center electric dipole (ED) or magnetic dipole (MD) point source located a distance 0.1 from the origin in the direction $\boldsymbol{p}(30^\circ, 90^\circ)$ with polarization vector $\boldsymbol{p}_{\mathrm{src}} = (1,1,0)^{\mathrm{T}}$, leading to the boundary conditions (1.8)–(1.10). The exact scattered field (and hence far field) is known for this point source scattering problem. We measure the error between a known function $\boldsymbol{u}$ (far field) and an approximation $\boldsymbol{u}_n$ on ∂B using the relative maximum error function

$$\text{Relative Error} = \max_{\hat{\boldsymbol{x}}\in\partial B}\left\{\sum_{\tilde{k}=1}^{3} \mid \boldsymbol{e}_{\tilde{k}}^{\mathrm{T}}[\boldsymbol{u}(\hat{\boldsymbol{x}}) - \boldsymbol{u}_n(\hat{\boldsymbol{x}})] \mid\right\} \Bigg/ \max_{\hat{\boldsymbol{x}}\in\partial B}\left\{\sum_{\tilde{k}=1}^{3} \mid \boldsymbol{e}_{\tilde{k}}^{\mathrm{T}}\boldsymbol{u}(\hat{\boldsymbol{x}}) \mid\right\}.$$

For comparison with results in [33] we also use the relative error in the RMS norm (measured in decibels)

$$\text{RMS error} = \left\{\frac{1}{4\pi}\int_{\partial B}[10\log_{10}\boldsymbol{u}(\hat{\boldsymbol{x}}) - 10\log_{10}\boldsymbol{u}_n(\hat{\boldsymbol{x}})]^2\,\mathrm{d}s(\hat{\boldsymbol{x}})\right\}^{1/2}.$$

We numerically approximate these errors at over 1300 points in ∂B. To demonstrate the convergence of our algorithm for plane wave scattering by non-spherical obstacles, we tabulate values of the bistatic RCS for various observation angles.

The number of unknowns $N = 2(n+1)^2 - 2$ required to solve a given scattering problem depends on the shape of the scatterer and the size of the scatterer relative to the wavelength $\lambda = 2\pi/k$ of the incident wave. Our demonstration scattering problems (obstacle description and relative-size) are listed in Table 1. The non-spherical scatterers are as shown in Fig. 2.

Our experiments were performed using a parallel version of our algorithm on a two node (8 socket) cluster with 2 GHz dual core Opteron (DcOp) processors. The maximum value of n that we use in our experiments is $n = 165$ (due to memory limitations) and the incident frequency in our experiments is chosen accordingly. When $n = 165$ our linear systems have only $N = 55,110$ unknowns and so we are able to present results using parallel direct solves. The ability to use direct solves is a considerable advantage for monostatic RCS computations, where we solve with one matrix but more than 2000 right hand sides. We remark that to obtain comparable results with algorithms in [17,18] would require more than $1.5N = 82,650$ unknowns, which could not be realized on the cluster that we use for the experiments in this paper.

The tables below demonstrate the high-order convergence of our algorithm for medium frequency scattering, with diameter up to 48λ (which in some literature is considered to be a very large three-dimensional problem even for acoustic scattering, as suggested by the title and numerical experiments in [2]). Our algorithm (GH) in this paper has also been tested at lower frequencies with all of the obstacles in [17,18] with similar accuracy to that reported there in all cases.

We show in Table 2 that using $N = 55,100$ unknowns we are able to obtain higher accuracy than FISC for scattering by a sphere with diameter 48 times the incident wavelength, even though we use only about *two percent* of the unknowns (2,408,448) required to obtain 0.33 dB RMS error using FISC [33, p. 29].

Results in Table 2 demonstrate that one may get higher accuracy in the far field induced by a point source than for that induced by a plane wave with the same frequency. Hence a convergence study of both point source and plane wave cases is necessary to demonstrate the performance of scattering algorithms. Accordingly, for non-spherical scatterers, we give point source far field error results in Tables 3, 4 and tabulate converging simulated bistatic RCS values for plane wave scattering in Tables 5–8.

Table 1
List of demonstration objects

Object	Sphere	Bean	Fount	Submarine	Erythrocyte
Diameter	48λ	30λ	30λ	30λ	40λ

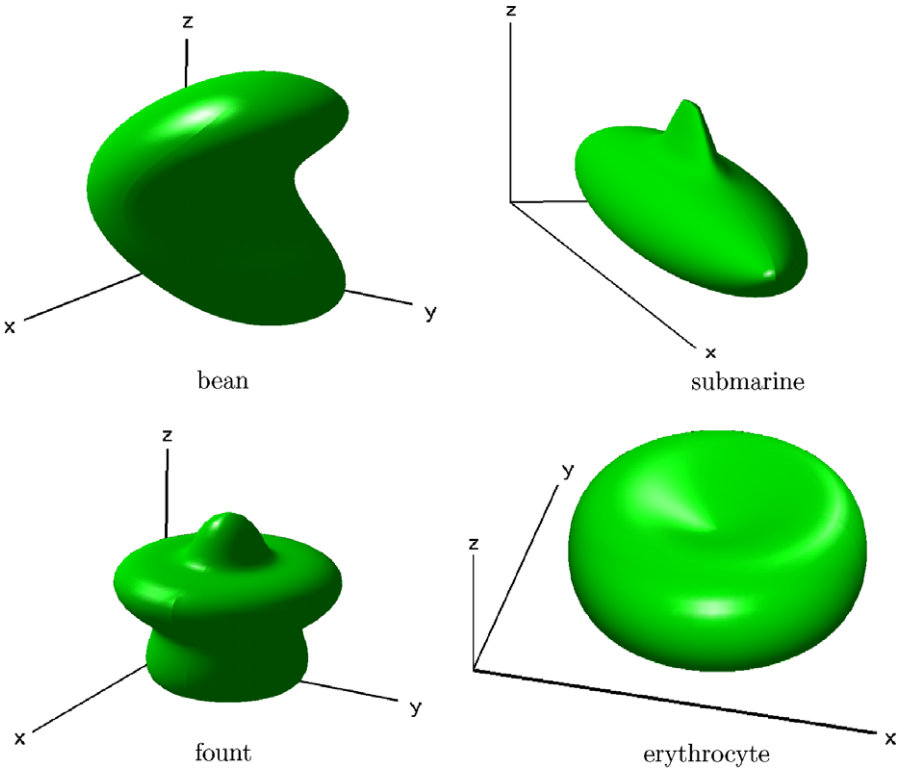

Fig. 2. Perfectly conducting scatterers used in our experiments.

Table 2
RMS error for GH (using GMRES) and FISC [33] for scattering by a sphere with diameter 48λ

Algorithm	Unknowns	MD RMS Err.	ED RMS Err.	PW RMS Err.
GH	48,670 ($n = 155$)	2.9e−11	1.9e−11	9.9e−02
FISC	2,408,448	–	–	3.3e−01
GH	51,840 ($n = 160$)	–	–	3.7e−03
GH	55,110 ($n = 165$)	–	–	5.9e−05

Table 3
Error in approximation to radiating field from point source

n	bean(30λ) $k = 47.1239$ MD Rel. Err.	bean(30λ) $k = 47.1239$ ED Rel. Err.	fount(30λ) $k = 78.5398$ MD Rel. Err.	fount(30λ) $k = 78.5398$ ED Rel. Err.
150	6.73e−04	9.09e−04	2.41e−06	1.18e−06
155	5.04e−05	7.54e−05	3.70e−07	2.08e−07
160	6.03e−06	7.87e−06	2.98e−07	1.45e−07

In [6, p. 104], using a fast high-order algorithm for scalar *acoustic scattering* by a bean obstacle with diameter 30 times the incident wavelength, 617, 910 unknowns were used to obtain accuracy less than that in Table 3 with $n = 155$. The CPU time required for a *single incident direction* in [6, p. 104] is about 80 h just for linear

Table 4
Error in approximation to radiating field from point source

n	sub(30λ) $k = 9.4248$ MD Rel. Err.	sub(30λ) $k = 9.4248$ ED Rel. Err.	ery(40λ) $k = 39.8932$ MD Rel. Err.	ery(40λ) $k = 39.8932$ ED Rel. Err.
150	4.94e−04	2.59e−04	1.43e−04	1.02e−04
155	2.59e−04	1.40e−04	5.56e−05	4.74e−05
160	7.42e−05	4.44e−05	2.26e−05	2.15e−05

Table 5
Computed bistatic RCS for incident wave $\hat{\boldsymbol{d}}_0 = -\boldsymbol{p}(\pi/2, \pi/2)$ with HH polarization for observation points in the horizontal plane with azimuth ϕ

n	bean(30λ) $k = 47.1239$ $\phi = 0.0°$	bean(30λ) $k = 47.1239$ $\phi = 60.0°$	bean(30λ) $k = 47.1239$ $\phi = 120.0°$	bean(30λ) $k = 47.1239$ $\phi = 180.0°$
150	11.32140391	15.07447877	15.07447880	11.32140392
155	11.32145461	15.07447142	15.07447142	11.32145464
160	11.32145841	15.07446793	15.07446794	11.32145840

Table 6
Computed bistatic RCS for incident wave $\hat{\boldsymbol{d}}_0 = -\boldsymbol{p}(\pi/2, \pi/2)$ with HH polarization for observation points in the horizontal plane with azimuth ϕ

n	fount(30λ) $k = 78.5398$ $\phi = 0.0°$	fount(30λ) $k = 78.5398$ $\phi = 60.0°$	fount(30λ) $k = 78.5398$ $\phi = 120.0°$	fount(30λ) $k = 78.5398$ $\phi = 180.0°$
150	8.234988913	5.047784768	5.047791415	8.235005411
155	8.234995275	5.047790111	5.047792074	8.234999861
160	8.235001560	5.047795533	5.047805101	8.235005031

Table 7
Computed bistatic RCS for incident wave $\hat{\boldsymbol{d}}_0 = -\boldsymbol{p}(\pi/2, 0)$ with HH polarization for observation points in the horizontal plane with azimuth ϕ

n	sub(30λ) $k = 9.4248$ $\phi = 0.0°$	sub(30λ) $k = 9.4248$ $\phi = 60.0°$	sub(30λ) $k = 9.4248$ $\phi = 120.0°$	sub(30λ) $k = 9.4248$ $\phi = 180.0°$
150	−17.25546467	−12.91421502	−3.984522645	23.87782796
155	−17.25560125	−12.91439235	−3.984531932	23.87782565
160	−17.25683322	−12.91438282	−3.984535724	23.87782207

Table 8
Computed bistatic RCS for incident wave $\hat{\boldsymbol{d}}_0 = -\boldsymbol{p}(0, 0)$ with VV polarization for observation points in the vertical plane with polar angle θ

n	ery(40λ) $k = 39.8932$ $\theta = 0.0°$	ery(40λ) $k = 39.8932$ $\theta = 60.0°$	ery(40λ) $k = 39.8932$ $\theta = 120.0°$	ery(40λ) $k = 39.8932$ $\theta = 180.0°$
150	41.39571841	11.61666797	9.801996741	56.93466410
155	41.39571993	11.61686887	9.801937614	56.93466411
160	41.39572008	11.61686949	9.801937292	56.93466412

iterative solves (with 18 iterations and 4 h and 28 min per iteration). For iterative solver based algorithms, the CPU time required for many incident directions is roughly the number of incident directions multiplied by the CPU time required for a single incident direction.

In Table 9 we give the total (set up + factorize + solve + RCS evaluation) CPU time required for vector *electromagnetic scattering* to compute the monostatic RCS of the bean obstacle with diameter 30 times the incident wavelength at 2402 incident directions using our algorithm with $n = 155$ (giving 48,670 unknowns)

Table 9
Total (set up + factorize + solve + RCS evaluation) time taken with $16 \times$ DcOp to compute the monostatic RCS of a bean shaped obstacle of diameter 30λ with 2402 incident directions

Algorithm	Unknowns	CPU time
GH	48,670 ($n = 155$)	10.5 h

Table 10
Error in approximation for scattering by a unit sphere with wave number close to an interior Maxwell eigenvalue at $k = 75.384956883881728$, simulated using $n = 95$

k	MD Rel. Err.	ED Rel. Err.	PW Rel. Err.
75.384	2.13e−10	4.89e−11	6.14e−10
75.38495	3.11e−08	6.00e−09	2.26e−09
75.3849568	2.54e−06	4.96e−07	1.70e−07
75.384956883	2.42e−04	4.69e−05	1.61e−05
75.38495688388	9.77e−02	1.91e−02	6.58e−03
75.3849568838817	4.42e−01	8.92e−02	3.07e−02
75.384956883881728	4.67e−01	9.41e−02	3.24e−02
75.3849568838818	5.48e−01	1.12e−01	3.86e−02
75.38495688389	2.73e−02	5.30e−03	1.82e−03
75.384956884	1.82e−03	3.50e−04	1.21e−04
75.3849569	1.34e−05	2.55e−06	8.89e−07
75.38496	6.86e−08	1.33e−08	4.71e−09
75.385	4.98e−09	9.54e−10	7.03e−10

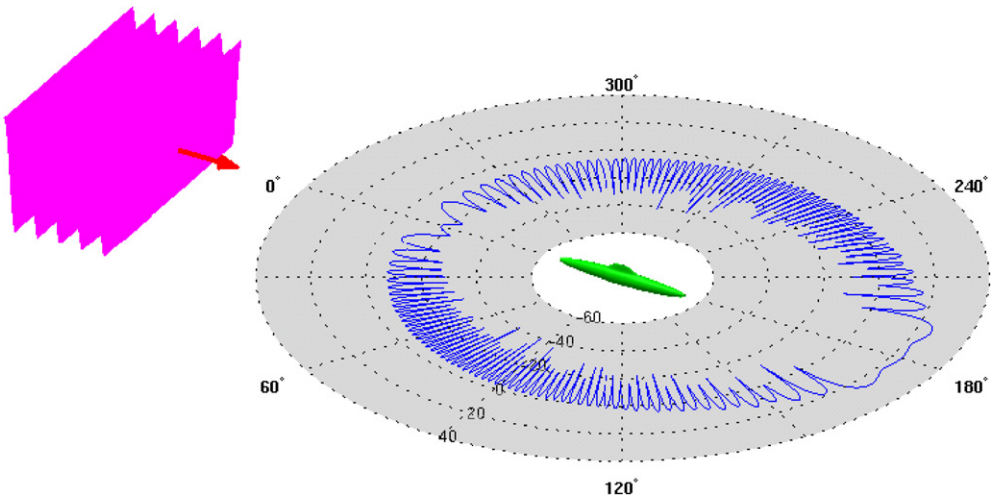

Fig. 3. Bistatic RCS of submarine with diameter 30λ for incident wave $\hat{\boldsymbol{d}}_0 = -\boldsymbol{p}(\pi/2, 0)$ with HH polarization, simulated using $n = 160$.

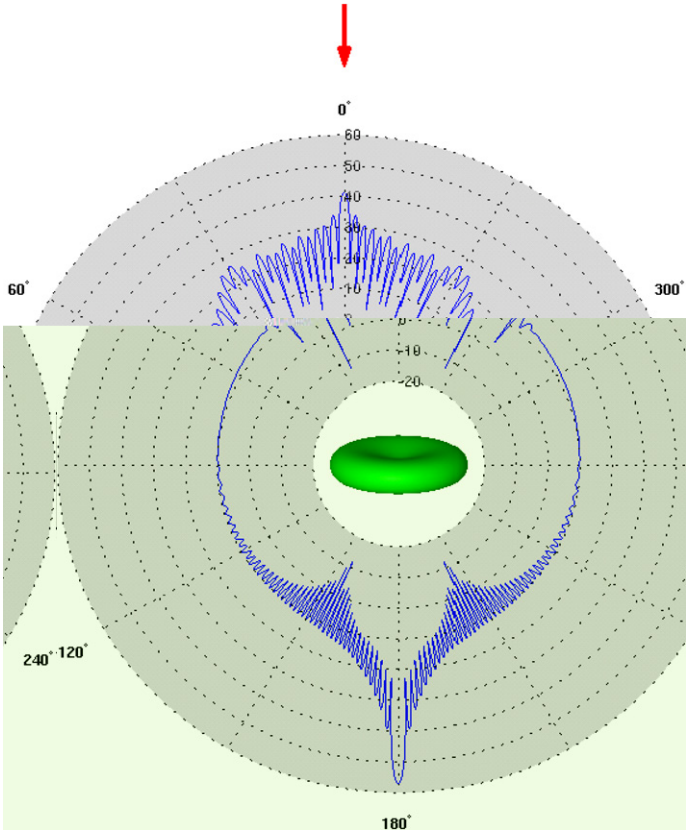

Fig. 4. Bistatic RCS of erythrocyte with diameter 40λ for incident wave $\hat{\boldsymbol{d}}_0 = -\boldsymbol{p}(0,0)$ with VV polarization, simulated using $n = 160$.

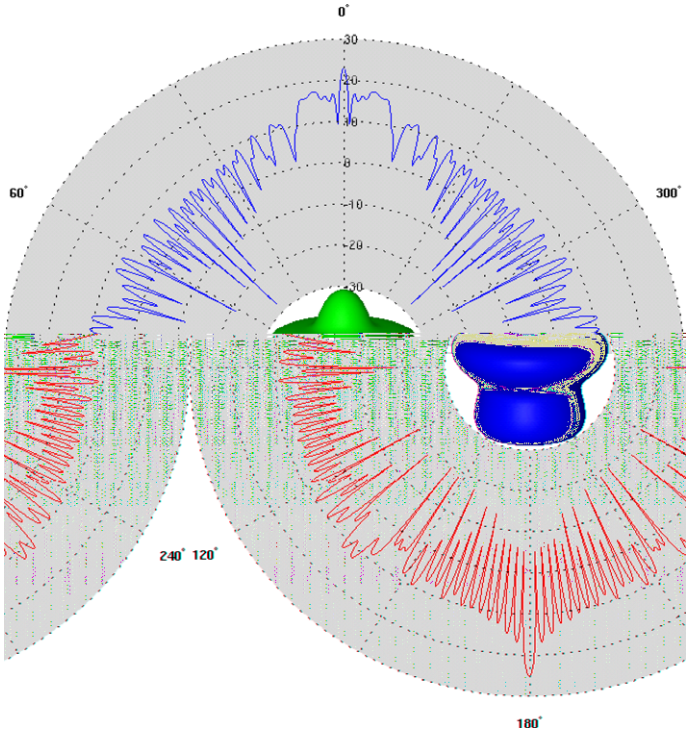

Fig. 5. Monostatic RCS of fount with diameter 30λ for incident wave with VV polarization, simulated using $n = 160$.

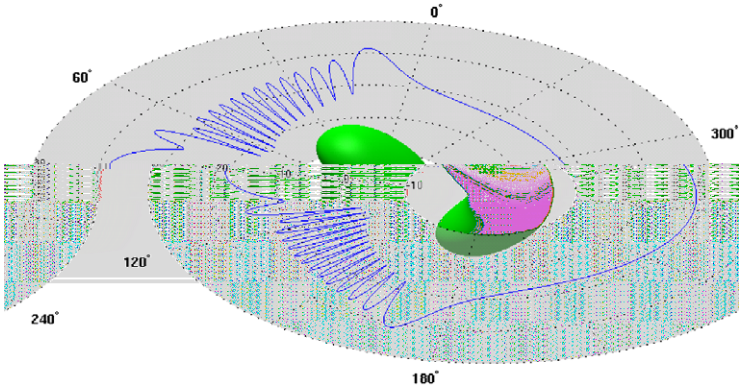

Fig. 6. Monostatic RCS of bean with diameter 30λ for incident wave with HH polarization, simulated using $n = 160$.

to obtain the accuracy detailed in Tables 3 and 5. For this case, using parallel direct solves we are able to solve the corresponding 2402 linear systems using 16 DcOp processors in less than 2.3 h after computing the LU factorization of the scattering matrix. Thus we are able to compute the monostatic RCS with over two thousand incident directions in about twice the time required for the present GH algorithm to compute the bistatic RCS. This is in contrast to electromagnetic scattering algorithms such as FISC, which are built on fast solvers and the fast multiple method with which such monostatic RCS computations would require approximately 2402 times as long as the corresponding bistatic RCS computation.

In Table 10 we demonstrate the robustness of our algorithm for wave numbers in the vicinity of an interior Maxwell eigenvalue. Although the integral equation (2.3) does not have a unique solution when k is an interior eigenvalue, we are able to obtain 8 digits accuracy in our approximate far field when k differs from the eigenvalue only in its eighth digit. In Figs. 3–6 we give polar plots of the bistatic and monostatic RCS obtained from the far field scattered by some of our test obstacles.

6. Conclusions

In this work we have utilized a new tangential basis that gives spectrally accurate approximation to simulate electromagnetic scattering by perfect conductors using only about twice as many unknowns as related acoustic scattering algorithms, and considerably fewer unknowns than industrial standard algorithms. We have demonstrated that this reduction in unknowns allows solution of problems at up to one hundred percent higher frequency than was possible using previous spectral Galerkin methods for electromagnetic scattering. These problems can be solved using direct solvers because of the relatively small number of unknowns. This is a particular advantage for monostatic RCS and BIE based T-matrix computations where one must solve linear systems with the same matrix but with hundreds or thousands of right hand sides.

Acknowledgments

Support of the Australian Research Council is gratefully acknowledged.

References

[1] G.E. Antilla, N.G. Alexopoulos, Scattering from complex three-dimensional geometries by a curvilinear hybrid finite-element-integral equation approach, J. Opt. Soc. Am. A 11 (1994) 1445–1457.
[2] A. Bendali, Y. Boubendir, M. Fares, A FETI-like domain decomposition method for coupling finite elements and boundary elements in large-size scattering problems of acoustic scattering, Comput. Struct. 85 (2007) 526–535.
[3] O.P. Bruno, Fast, high-order, high-frequency integral methods for computational acoustics and electromagnetics, in: M. Ainsworth et al. (Eds.), Topics in Computational Wave Propagation Direct and Inverse Problems Series, Lecture Notes in Computer Science and Engineering, vol. 31, Springer, 2003.
[4] O.P. Bruno, C.A. Geuzaine, An $\mathcal{O}(1)$ integration scheme for three-dimensional surface scattering problems, J. Comput. Appl. Math. 204 (2007) 463–476.

[5] O.P. Bruno, C.A. Geuzaine, J.A. Monro, F. Reitich, Prescribed error tolerances within fixed computational times for scattering problems of arbitrarily high frequency: the convex case, Philos. Trans. R. Soc. Lond. Ser. A: Math. Phys. Eng. Sci. 362 (2004) 629–645.
[6] O.P. Bruno, L.A. Kunyansky, A fast, high-order algorithm for the solution of surface scattering problems: basic implementation, tests, and applications, J. Comput. Phys. 169 (2001) 80–110.
[7] L. Canino, J. Ottusch, M. Stalzer, J. Visher, S. Wandzura, Numerical solution of the Helmholtz equation in 2D and 3D using a high-order Nystrom discretization, J. Comput. Phys. 146 (1998) 627–663.
[8] D. Colton, R. Kress, Integral Equation Methods in Scattering Theory, Wiley, 1983.
[9] D. Colton, R. Kress, Inverse Acoustic and Electromagnetic Scattering Theory, Springer, 1998.
[10] V. Domínguez, I.G. Graham, V.P. Smyshlyaev, A hybrid numerical-asymptotic boundary integral method for high-frequency acoustic scattering, Numer. Math. 106 (2007) 471–510.
[11] O. Dorn, D. Lesselier, Level set methods for inverse scattering, Inverse Problems 22 (2006) R67–R131.
[12] O. Dorn, D. Lesselier, Level set techniques for structural inversion in medical imaging, in: J.S. Suri, A. Farag (Eds.), Deformable Models: An Application in Biomaterials and Medical Imagery, Springer, 2007, pp. 61–90.
[13] F. Ecevit, F. Reitich, Analysis of multiple scattering iterations for high-frequency scattering problems. I: The two-dimensional case, Preprint, 2006.
[14] W. Freeden, T. Gervens, M. Schreiner, Constructive Approximation on the Sphere, Oxford University Press, 1998.
[15] K.A. Fuller, D.W. Mackowski, Electromagnetic scattering by compound spherical particles, in: M.I. Mishchenko, J.W. Hovenier, L.D. Travis (Eds.), Light Scattering by Nonspherical Particles, Academic Press, 2000, pp. 225–272 (Chapter 8).
[16] M. Ganesh, I.G. Graham, A high-order algorithm for obstacle scattering in three dimensions, J. Comput. Phys. 198 (2004) 211–242.
[17] M. Ganesh, S.C. Hawkins, A spectrally accurate algorithm for electromagnetic scattering in three dimensions, Numer. Algor. 43 (2006) 25–60.
[18] M. Ganesh, S.C. Hawkins, A hybrid high-order algorithm for radar cross section computations, SIAM J. Sci. Comput. 29 (2007) 1217–1243.
[19] M. Ganesh, S. Langdon, I. Sloan, Efficient evaluation of highly oscillatory acoustic scattering surface integrals, J. Comput. Appl. Math. 204 (2007) 363–374.
[20] C. Geuzaine, O. Bruno, F. Reitich, On the $\mathcal{O}(1)$ solution of multiple-scattering problems, IEEE Trans. Magnet. 41 (2005) 1488–1491.
[21] D. Goldberg-Zimring, I. Talos, J. Bhagwat, S. Haker, P.M. Black, K.H. Zou, Statistical validation of brain tumor shape approximation via spherical harmonics for image-guided neurosurgery, Acad. Radiol. 12 (2005) 459–466.
[22] J. Hellmers, E. Eremina, T. Wriedt, Simulation of light scattering by biconcave Cassini ovals using the nullfield method with discrete sources, J. Opt. A: Pure Appl. Opt. 8 (2006) 1–9.
[23] G.C. Hsiao, P.B. Monk, N. Nigam, Error analysis of a finite element-integral equation scheme for approximating the time-harmonic Maxwell system, SIAM J. Numer. Anal. 40 (2002) 198–219.
[24] E.F. Knott, J.F. Shaeffer, M.T. Tuley, Radar Cross Section, SciTech Publishing Inc., 2004.
[25] S. Langdon, S.N. Chandler-Wilde, A wave number independent boundary element method for an acoustic scattering problem, SIAM J. Numer. Anal. 43 (2006) 2450–2477.
[26] P.A. Martin, Multiple Scattering: Interaction of Time-Harmonic Waves with N Obstacles, Cambridge University Press, 2006.
[27] R.B. Melrose, M.E. Taylor, Near peak scattering and the corrected Kirchhoff approximation for a convex obstacle, Adv. Math. 55 (1985) 242–315.
[28] M.I. Mishchenko, L.D. Travis, D.W. Mackowski, T-matrix computations of light scattering by nonspherical particles: a review, J. Quant. Spectrosc. Radiat. Transfer 55 (1996) 535–575.
[29] P. Monk, Finite Element Methods for Maxwell's Equations, Oxford University Press, 2003.
[30] T. Nousiainen, G.M. McFarquhar, Light scattering by quasi-spherical ice crystals, J. Atmos. Sci. 61 (2004) 2229–2248.
[31] R. Reimer, Hyperinterpolation on the sphere at the minimal projection order, J. Approx. Theory 103 (2000) 272–286.
[32] I.H. Sloan, R.S. Womersley, Constructive polynomial approximation on the sphere, J. Approx. Theory 103 (2000) 91–118.
[33] J.M. Song, C.C. Lu, W.C. Chew, S.W. Lee, Fast Illinois Solver Code (FISC), IEEE Antennas Propag. Mag. 40 (1998) 27–34.
[34] J.A. Stratton, Electromagnetic Theory, McGraw-Hill, 1941.
[35] L. Tsang, J.A. Kong, K. Ding, Scattering of Electromagnetic Waves: Theories and Applications, Wiley, 2000.
[36] H.C. van de Hulst, Light Scattering by Small Particles, Dover Publications Inc., 1981.
[37] B. Veihelmann, T. Nousiainen, M. Kahnert, W.J. van der Zande, Light scattering by small feldspar particles simulated using the Gaussian random sphere geometry, J. Quant. Spectrosc. Radiat. Transfer 100 (2005) 393–405.
[38] E.B. Wilson, Vector Analysis: A Text-Book for the Use of Students of Mathematics and Physics; Founded Upon the Lectures of J. Willard Gibbs, Springer, 1998.
[39] A.C. Woo, H.T. Wang, M.J. Schuh, M.L. Sanders, Benchmark radar targets for the validation of computational electromagnetics programs, IEEE Antennas Propag. Mag. 35 (1993) 84–89.
[40] T. Wriedt, J. Hellmers, E. Eremina, R. Schuh, Light scattering by single erythrocyte: comparison of different methods, J. Quant. Spectrosc. Radiat. Transfer 100 (2006) 444–456.
[41] A.D. Zacharopoulos, S.R. Arridge, O. Dorn, V. Kolehmainen, J. Sikora, 3D shape reconstruction in optical tomography using spherical harmonics and BEM, J. Electromagn. Waves Appl. 20 (2006) 1827–1836.
[42] A.D. Zacharopoulos, S.R. Arridge, O. Dorn, V. Kolehmainen, J. Sikora, Three-dimensional reconstruction of shape and piecewise constant region values for optical tomography using spherical harmonic parametrization and a boundary element method, Inverse Problems 22 (2006) 1509–1532.